J. Mech. Phys. Solids 153 (2021) 104491

Contents lists available at ScienceDirect

Journal of the Mechanics and Physics of Solids

journal homepage: www.elsevier.com/locate/jmps

Nonlinear elastodynamic behavior of intact and fractured rock under in-situ stress and saturation conditions

Prabhakaran Manogharan [a], Clay Wood [b], Chris Marone [b], Derek Elsworth [c], Jacques Rivière [a], Parisa Shokouhi [a,*]

[a] Department of Engineering Science and Mechanics, The Pennsylvania State University, USA
[b] Department of Geosciences, The Pennsylvania State University, USA
[c] Energy and Mineral Engineering and Energy Institute, The Pennsylvania State University, USA

ARTICLE INFO

Keywords:
Nonlinear elastodynamic response
Contact acoustic nonlinearity
Fracture mechanics
Dynamic acousto-elastic testing

ABSTRACT

We probe mechanisms controlling the nonlinear elastodynamic response of intact and fractured rock under both fluid-saturated and dry conditions. We present the results of dynamic acoustoelastic testing (DAET) on Westerly granite in three states: dry-intact, dry-fractured and saturated-fractured to study the influence of in-situ stress, fracture and saturation state on nonlinear elastodynamic behavior. Each sample is tested at effective normal stresses from 10 to 20 MPa. Dynamic stresses of prescribed amplitudes (0.2 – 1.0 MPa) and frequencies (0.1, 1 and 10 Hz) are superimposed on the static stress field, while pulsed ultrasonic waves transit the sample and monitor stress-induced changes in wave velocity and spectral amplitude to infer sample's elastodynamic nonlinearity. Surprisingly, dry-intact rock exhibits higher nonlinearity than dry-fractured sample at all stress levels. We use numerical simulations to argue that the reduced nonlinearity is a result of the non-uniform strain field post fracture with highly strained regions on the fracture plane and weakly-strained regions in the surrounding host-rock, both leading to a nonlinearity reduction. In addition, we demonstrate that the saturated sample is less nonlinear than the dry intact except at 10 MPa normal stress, where the fracture is fairly open. The expected decrease in nonlinearity is due to increased fracture stiffness by the presence of fluid within the fracture interface. The reported in-situ measured nonlinear elastic properties along with their frequency dependencies will be of practical importance in predicting poromechanical properties of rock masses and will facilitate comparisons between the observations made in the laboratory and field scales.

1. Introduction

The nonlinear elastic properties of rocks can be exploited to understand their fluid flow and poromechanical response and frictional constitutive behavior - all exerting key controls on engineered and natural processes in the subsurface (Berkowitz, 2002; Candela et al., 2015; Elkhoury et al., 2011, 2006). The nonlinear elastodynamic response of fractured rock also encodes crucial information about the microscopic contact features of the fracture such as interface roughness, aperture and crack density (Bandis et al., 1983; Brown, 1987; Hudson et al., 1996; Nara et al., 2011). Our recent controlled laboratory experiments suggest a coupling between the changes in wave

* Corresponding author.
E-mail address: parisa@engr.psu.edu (P. Shokouhi).

https://doi.org/10.1016/j.jmps.2021.104491
Received 26 November 2020; Received in revised form 30 April 2021; Accepted 7 May 2021
Available online 16 May 2021

velocity during dynamic stressing and permeability transients (Shokouhi et al., 2020). A better understanding of the nonlinear elastodynamic behavior of fractured rock in different states is essential in utilizing the complex coupling between nonlinear stiffness and permeability to help infer or even predict the poromechanical properties of fractured rock (Nara et al., 2011; Pyrak-Nolte and Nolte, 2016; Shokouhi et al., 2020).

Compared to metals, even when macroscopically intact, rocks exhibit strong elastodynamic nonlinearity. Rocks - like other nonlinear mesoscopic elastic materials - exhibit several interesting nonlinear behaviors (Guyer and Johnson, 2009). These include stress-strain dependent elastic properties, transient elastic softening upon dynamic stressing known as conditioning (Renaud et al., 2013; Renaud et al., 2012, 2011; Sens-Schönfelder and Eulenfeld, 2019), hysteresis (Holcomb, 1981) and slow dynamics, the slow recovery of stiffness post perturbation (Sens-Schönfelder et al., 2018; Ten Cate and Shankland, 1996; TenCate et al., 2000). The observed nonlinearity is attributed to rocks' inherent heterogeneous microstructure and grain-interface stiffness mismatch. A

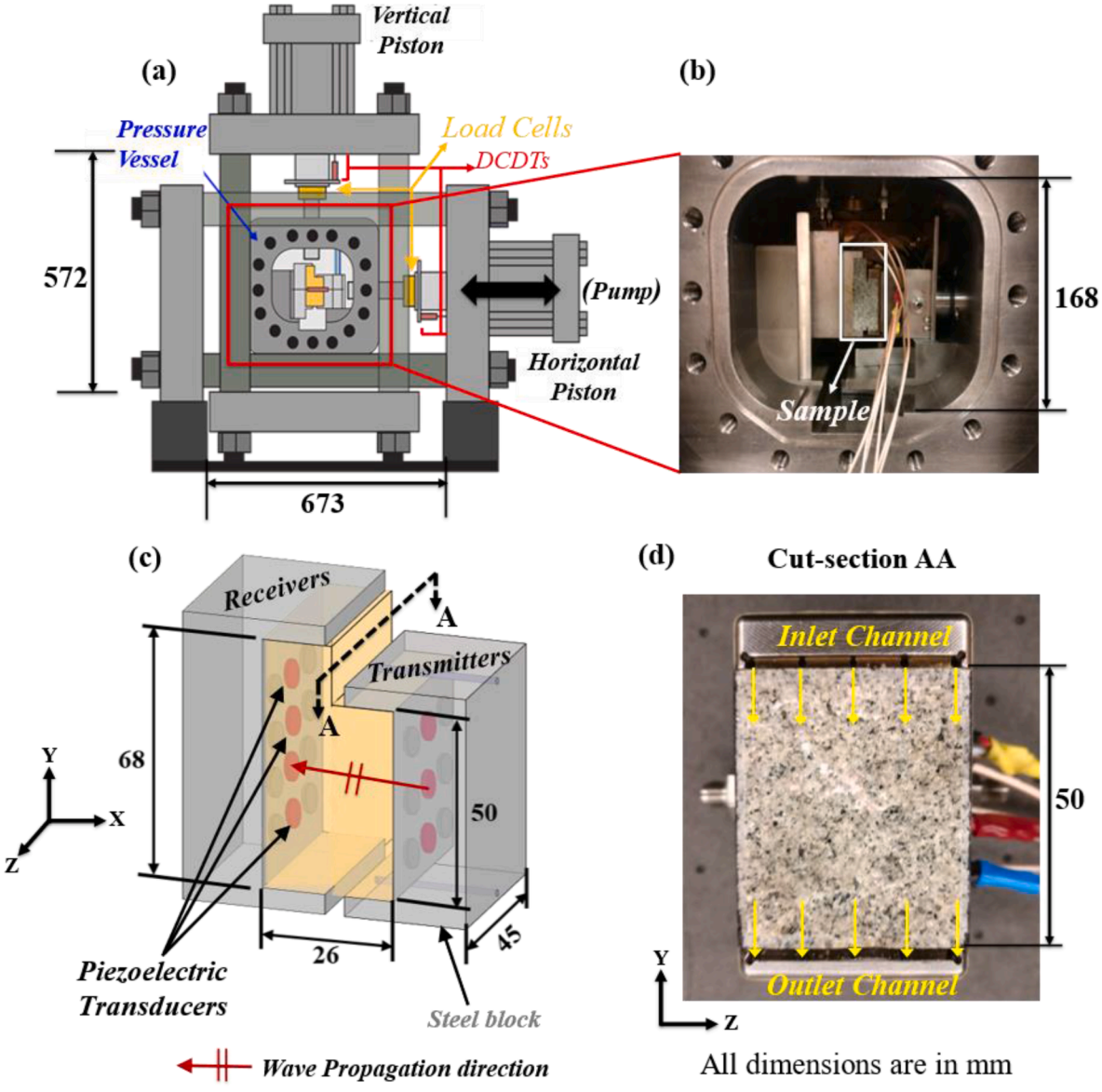

Figure 1. Experimental setup: (a) Schematic representation of the biaxial loading apparatus showing the horizontal piston applying fracture-normal stress to the sample as inserted within the pressure vessel. Displacements and stresses are measured using Direct-Current Displacement Transducers (DCDTs) and load cell. The pump direction *(i.e., normal stress oscillations)* is shown with the thick double-headed arrow; (b) Zoomed-in photograph of the pressure vessel with front door removed showing the sample, steel loading platens and loading configuration; (c) Schematic representation of L-shaped sample placed between the steel blocks with embedded ultrasonic piezoelectric transducers to probe the evolution of wave velocity before, during and after the dynamic oscillations. The red arrow marks the wave propagation direction; (d) Fractured sample within steel platen showing fluid supply channels (Photograph taken across the cut-section AA shown in Fig. 1c).

technique called dynamic acoustoelastic testing (DAET) has been recently employed to study the nonlinear elastodynamic properties of rocks. In DAET, nonlinearity is quantified by measuring changes in a high-frequency *probe* wave speed and attenuation caused by a low-frequency *pump*. DAET is analogous to (static) acoustoelastic testing (Winkler and Liu, 1996; Winkler and McGowan, 2004) except that the quasi-static loading is replaced by the dynamic low-frequency pump. DAET allows studying different aspects of rocks' nonlinearity behavior. Also, in contrast to resonance-based methods (Haupert et al., 2011; Johnson et al., 2009; Remillieux et al., 2016; Rivière et al., 2014; Van Den Abeele et al., 2000), DAET results are local, specific to the location of the probe and the corresponding wave path (Lott et al., 2016; Renaud et al., 2016; Rivière et al., 2013). Finally, the DAET setup and observations in the laboratory settings (e.g., Shokouhi et al., 2020, 2017a) are transportable to larger scales (Renaud et al., 2014). In the field, the nonlinear elastic response of near sub-surface has been evaluated using DAET-style approaches, where the ground motion generated with a large shaker truck sets the strain pump (Renaud et al., 2014). At even larger scales, a sudden drop in seismic wave velocity (probe) near and on faults during earthquakes (pump) followed by a post-seismic recovery (Brenguier et al., 2014, 2008; Gassenmeier et al., 2016; Nakata and Snieder, 2011; Niu et al., 2008; Rubinstein, 2004; Wegler et al., 2009) resembles laboratory DAET observations (e.g., Shokouhi et al., 2020, 2017a) and is likely due (at least in part) to the nonlinear elastic nature of the shallow crust.

DAET observations of rocks in the laboratory have so far been limited to intact samples (Renaud et al., 2011, Renaud et al., 2013a, Renaud et al., 2013b, Rivière et al., 2013, Rivière et al., 2015, Rivière et al., 2016, Shokouhi et al., 2017a), although acoustoelasticity of fractured rocks has been reported under quasi-static stress conditions (Lubbe, 2005; Pyrak-Nolte et al., 1990). We build upon these previous studies and use a DAET-like setup to investigate, for the first time, the effect of a fracture interface in modifying the nonlinear elastodynamic behavior of Westerly granite under different stress conditions. While the nonlinearity of intact rocks arises from the distribution of soft grain boundaries and microcracks (R. A. Guyer and P. A. Johnson, 2009; Rivière et al., 2015) the nonlinear elastodynamic response of fractured rock also includes the contact acoustic nonlinearity (CAN) at the rough fractured interface. In addition, we study the effect of saturation on fracture response under dynamic stressing. These observations are then used in physics-based models to understand the information encoded in the response and define the respective roles of ambient conditions (intact/fractures and dry/saturated).

2. Experimental procedure

We measure the nonlinear elastodynamic response to dynamic stress perturbations for Westerly granite samples using a true triaxial loading apparatus (Elkhoury et al., 2011; Samuelson et al., 2009). The machine is servo-controlled and equipped with hydraulic pistons to apply vertical and horizontal loads in either displacement- or load-control (Fig. 1). We use the horizontal piston to apply constant stress normal to the fracture plane. Fig. 1b shows the loading configuration used for the dry experiments. A flexible rubber jacket (not shown) is used for the fluid-saturated experiment. In both cases, the sample is loaded within a pressure vessel. The fracture-normal displacement is measured with a direct current displacement transducer (DCDT) (Trans-Tek Inc., series 240) mounted between the load frame and the horizontal piston (Fig. 1a). In addition, a DCDT is placed directly across the fracture inside the pressure vessel to accurately measure changes in sample thickness or fracture-normal displacement to a resolution of $\pm 0.1\mu m$. Normal loads are measured using a load cell attached to the horizontal piston with an accuracy of $\pm 5N$.

Samples of Westerly granite are machined into L-shaped blocks of dimension $68 \times 50 \times 45 \times 26$ mm as shown in Fig. 1c. The L-shaped samples are placed between steel loading platens with embedded ultrasonic piezoelectric transducers (PZTs) (APC International Ltd, P-wave polarized, 6.5 mm in diameter with a nominal center frequency of 500 kHz) as shown in Fig. 1c. One of the steel blocks has fluid supply channels at the top and bottom to saturate the sample and to allow flow along the fracture (Fig. 1d). The fluid lines are connected to servo-controlled pressure intensifiers. Linear variable differential transformers (LVDTs) (Trans-Tek Inc., series 220) mounted on the intensifier pistons and pressure transducers are used to control the fluid flow and confining pressures, respectively. Mechanical data (displacements, stresses and pressures) are digitally recorded at 10 kHz with a 16-channel 24-bit analog-to-

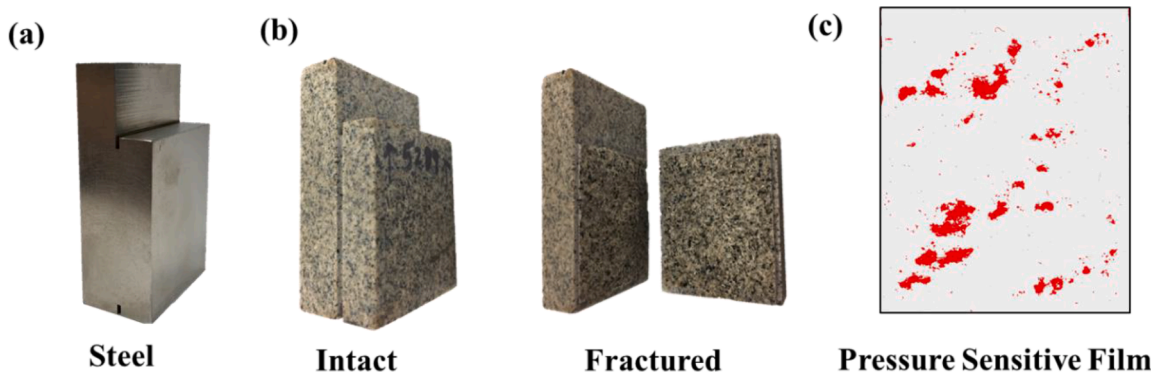

Figure 2. (a) L-shaped steel sample used for calibration; (b) Westerly granite sample first intact then fractured into two halves. The fracture was created using a Brazilian test apparatus; (c) Footprints of the contact areas on a pressure sensitive film showing the distribution of *true contacts* in red at a normal stress of 15 MPa (experiment p5379).

digital converter and moving-averaged to 0.1-1 kHz for storage. In all our experiments, once the required normal stress level (10-20 MPa) is reached, ultrasonic pulses are generated and recorded by a Research Ultrasound system (Verasonics) at a rate of 25 MHz. The mechanical and ultrasonic data are synchronized to analyze the stress-induced changes in the velocity and spectral amplitude. Details of the ultrasonic pulse excitation and data analysis are explained in Section 2.2.

Before performing the experiments with rock, a baseline measurement is conducted on an intact steel replicate of identical size and shape to the rock sample (Fig. 2a) – to measure the overall nonlinearity of the loading system and ensure that they are small relative to rock nonlinearity. The baseline measurement on the steel sample with very small materials nonlinearity (provided in the supplementary information - Fig. S1) confirms that despite the complexity of the test apparatus, the system nonlinearity in our experimental setup is minimal and therefore, the measured stress-induced changes in wave velocity and amplitude can be attributed directly to the nonlinearity of the samples. Next, we perform experiments on the Westerly Granite sample under three different conditions: (1) dry-intact, (2) dry-fractured, then (3) saturated-fractured (Figs. 2 and 3). For the intact experiment, the sample is installed inside the loading apparatus (Fig. 1b) then loaded to the first stress level (10 MPa). The dynamic stress oscillation protocol (see Section 2.1 and Fig. 3d) is executed by oscillating the horizontal piston of the loading apparatus at different amplitudes and frequencies ('the DAET

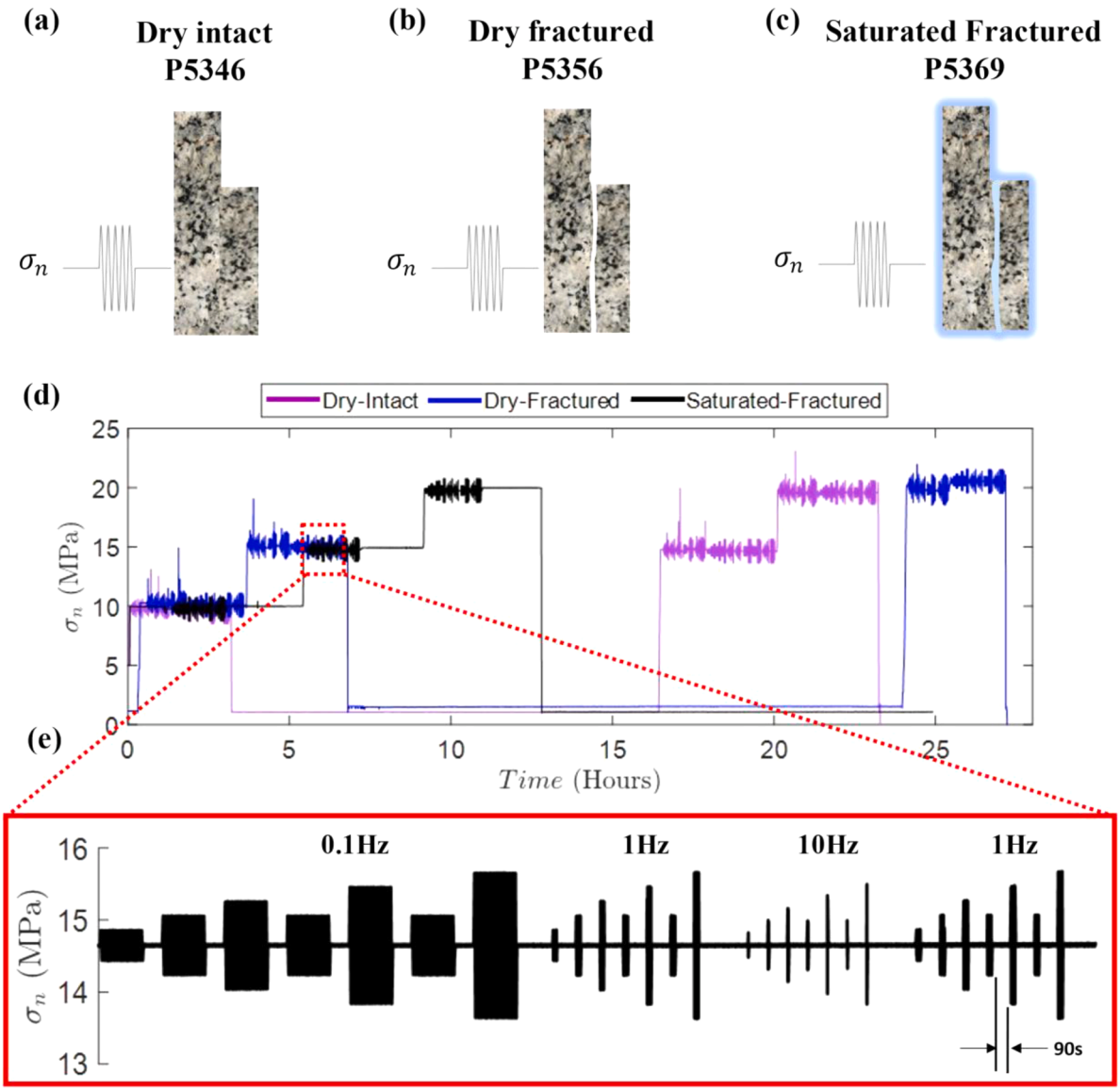

Figure 3. Schematic representation of L-shaped Westerly granite sample in three states: (a) Dry-intact; (b) Dry-fractured and (c) Saturated-fractured; (d) Loading history of dry-intact, dry-fractured and saturated-fractured experiments. (e) Overview of the imposed normal stress oscillation amplitudes and frequencies at 15 MPa normal stress. The hold time between subsequent oscillations is 90 seconds. Note that the 1-Hz oscillation amplitudes are repeated twice to test for reproducibility. The very same series of oscillations with similar amplitudes and frequencies are applied to the sample in different configurations and at different normal stress levels.

pump'). Ultrasonic pulses ('the DAET probe') are then continuously generated and recorded before, during and after the oscillation sets. A similar protocol is followed at the next two stress levels (15 and 20 MPa). For the second experiment, the intact sample is fractured outside the pressure vessel using a Brazilian test apparatus (a small amount of wear material at the fractured interface was lost while fracturing). The two fractured halves shown in Fig. 2b are then re-mated, positioned within the apparatus and then loaded to the desired normal stress. At each normal stress, the sample is pumped and probed following a predefined stress oscillation protocol (Fig. 3). The dry-unfractured and dry-fractured experiments are conducted on unjacketed samples. The saturated-fractured sample is jacketed and subject to a confining pressure of 3 MPa and pore fluid pressure on the fracture of 1.4 MPa; both are servo-controlled and kept constant. The applied horizontal force is adjusted to produce effective fracture normal stresses of 10, 15 and 20 MPa. To allow comparisons, the effective normal stresses, oscillation amplitudes, and frequencies are all consistent among the three sample conditions.

Additionally, the *true* distribution of contact area on the re-mated fracture is measured using pressure-sensitive films (Fujifilm) before the experiments on the fractured sample. The contact "footprints" on the films allow the size and spatial locations of the contact areas formed during the normal stress loading to be determined. The resulting contact "footprints" are digitized using an HD scanner (EPSON perfection 3200) with the converted images processed using a thresholding algorithm *via* ImageJ (Schneider et al., 2012) to estimate the true contact area. Fig. 2c shows an example of the processed pressure-sensitive film at a nominal normal stress of 15 MPa. We note that the processed image can be further analyzed to provide stress distributions recovered from the color/hue of the pressure-sensitive film (Selvadurai and Glaser, 2017).

2.1. Dynamic stress oscillation protocol

We apply a set of oscillations after reaching the target stress: 10, 15 or 20 MPa. The load is ramped to the prescribed stress level within a few minutes after which, it is held constant before executing the oscillation protocol. The hold time is roughly 5 minutes at all stresses and sample conditions. At 10 MPa normal stress for saturated-fractured condition, the normal stress is held for ~1 hour while confining and pore pressures are increased to fully saturate the sample. Therefore, the effective stress hold time is still about 5 minutes. Fig. 3d shows the loading history of all the experiments appended together.

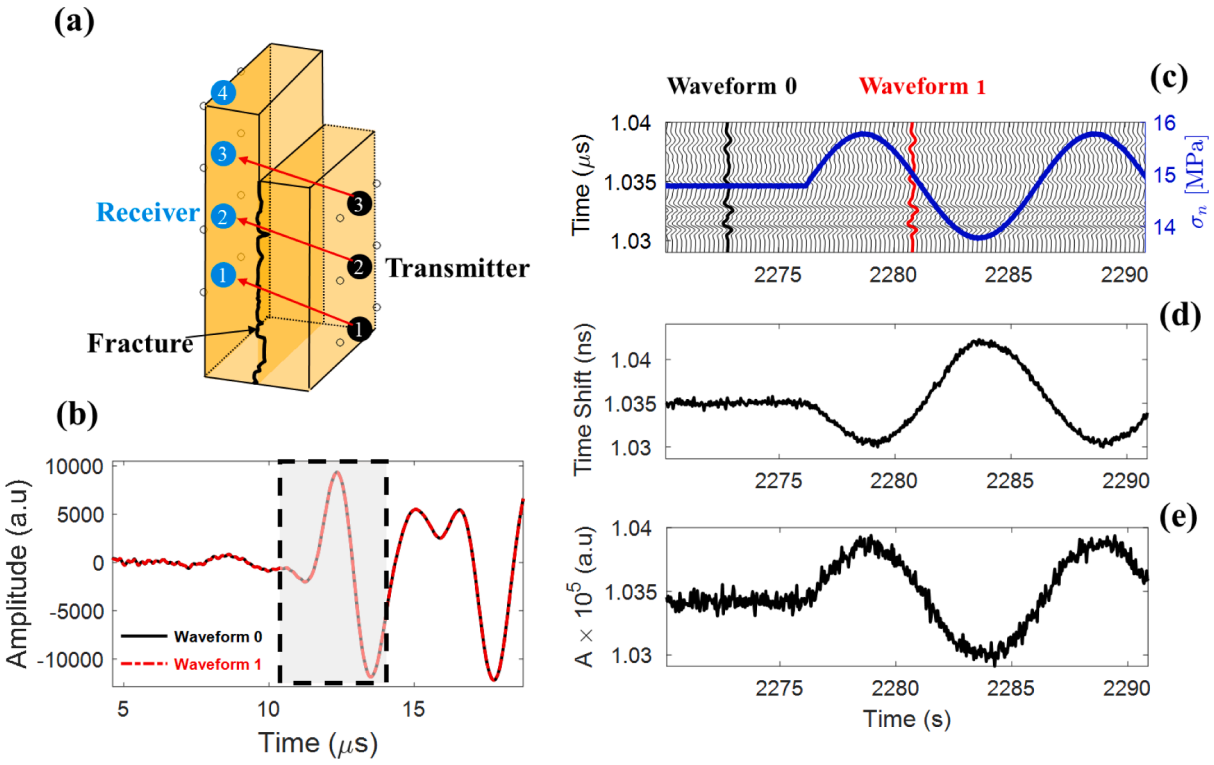

Figure 4. Example illustrating the procedure used to calculate the evolution of time shift (or wave velocity) and spectral amplitude due to the applied stress oscillations: (a) Schematic representation of the ultrasonic transmitters (T) and receivers (R) together with the wave paths for the T-R pairs considered in this study; (b) Transmitted ultrasonic wave pulses before (e.g., waveform #0) and during (e.g., waveform #1) the stress oscillation. The window used for cross-correlation extends from 9.7-14.2 μs as marked; (c) Imposed low-frequency normal stress oscillations (blue: amplitude of 1 MPa and frequency of 1 Hz) and superimposed ultrasonic waveforms recorded prior to and during the stress oscillation. The pulse repetition frequency is 5 kHz with only a subset (5%) of waveforms shown here for readability; (d) The resulting time shift and (e) spectral amplitude histories calculated from the ultrasonic waveforms. (data from experiment p5369)

Overview of the imposed series of oscillations used for all normal stress levels and sample configuration is shown in Fig. 3e. At each oscillation frequency (0.1Hz, 1Hz and 10Hz) we apply 20 cycles with the amplitude increasing from 0.2 MPa to 1 MPa. The 0.4-MPa oscillations are repeated twice in between larger amplitude oscillations (0.2; 0.4; 0.6; 0.4; 0.8; 0.4; 1) to study repeatability and possible permanent/inelastic changes in the medium caused by larger amplitude oscillations. In addition, the 1-Hz oscillation set is repeated to investigate the repeatability and reproducibility of the results. A 90-second hold time is allocated between oscillations.

2.2. Ultrasonic measurements and data processing

Ultrasonic pulses are continuously transmitted across the sample with a pulse repetition frequency (PRF) of 5 kHz throughout the experiment. Two arrays of piezoelectric transducers (PZTs) embedded in the steel loading platens hold the sample as shown in Fig. 1c. The transmitting PZT transducers are excited with half sine wave pulses (96 V; 500 kHz). Out of a total of nine transmitters (T) and twelve receivers (R), only three transmitters and four receivers in the center array of each block are activated (Fig. 4a). We focus on the results of transmitter (T) and receiver (R) pairs with a minimal vertical offset, namely T1-R1, T2-R2 and T3-R3 (see Fig. S2 in the supplementary section for steel block dimensions). Due to the complexity of the experimental setup, some of the T-R pairs did not function properly. Therefore, we report only the available T-R pair results: T1-R1 and T2-R2 for the dry-intact experiment, T3-R3 for the dry-fractured experiment and all three pairs for the saturated-fractured experiment.

Ultrasonic data processing entails calculating the evolution of (1) wave velocity and (2) amplitude over time: before, during and after imposing the stress oscillations. The details of the data analysis are illustrated in Fig. 4. Fig. 4c shows an example of the low-frequency stress perturbation superimposed by (a small subset of) the ultrasonic waveforms collected prior to and during the oscillation cycles. To estimate changes in ultrasonic wave velocity due to the imposed low-frequency oscillation, we first calculate the time

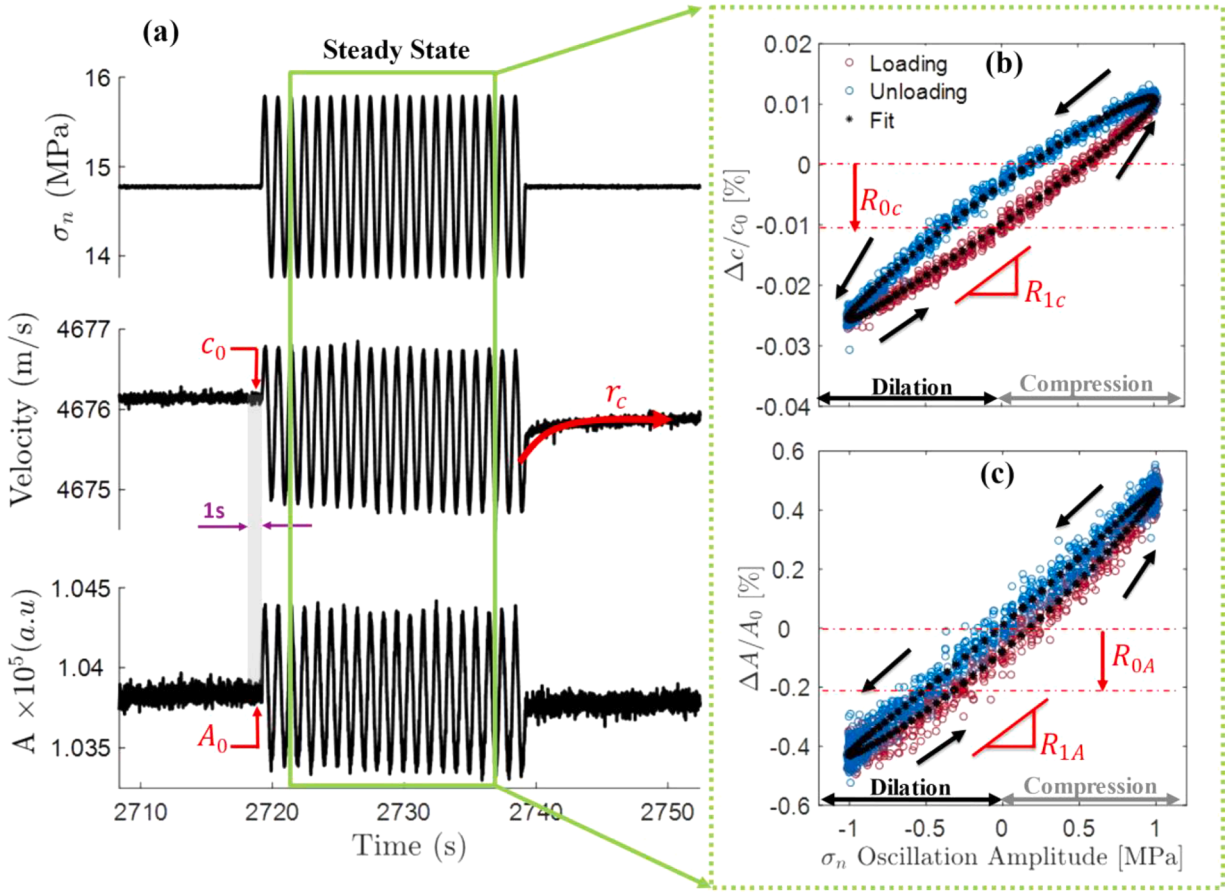

Figure 5. (a) Example of applied normal stress oscillations (amplitude = 1 MPa and frequency = 1 Hz) and resulting evolution of ultrasonic wave velocities and spectral amplitudes at 400 kHz for the T3-R3 transmitter-receiver pair. The pre-oscillation wave velocity (c_0) and spectral amplitude (A_0) is obtained by averaging wave velocity/spectral amplitude over a 1-second window preceding the oscillations. The recovery rate (r_c) of wave velocity post oscillations is shown schematically. (b) Velocity and (c) spectral amplitude *vs.* imposed dynamic stress amplitude during the marked time window (green box) together with the fit calculated using the projection procedure. The instantaneous drop in wave velocity and spectral amplitude (R_0), and wave velocity and spectral amplitude modulation during oscillations (R_1) are also shown schematically. (data from experiment p5369)

shift by cross-correlating each received ultrasonic signal (e.g., waveform n) with a reference waveform (waveform 0) within a pre-defined window. The reference waveform (waveform 0) is obtained by averaging 50 waveforms recorded during the unperturbed stress state. The location and size of the cross-correlation window are carefully selected such that the window includes the p-wave arrival and extends over at least one period as shown in Fig. 4b. The lag corresponding to the maximum cross-correlation gives the time shift between any waveform n and the reference waveform 0 (Fig. S3a). Given the second-order nature of these measurements, the calculated time shifts are often very small - on the order of 1 ns. The estimation of time shift is fine-tuned by fitting the peak of the cross-correlation function (passing through the peak and adjacent points on the either side of the peak) by a second-order polynomial (Fig. S3a). The modified time shift corresponds to the maximum of the parabola. Fig. 4d shows a plot of time shift versus time. To obtain the absolute arrival times, the measured (relative) time shift is added to the p-wave arrival time of the reference signal (waveform 0) estimated using a simple thresholding procedure. The wave velocity is then measured by dividing the initial thickness (26 mm) of the sample by the absolute arrival times (without accounting for the changes in the thickness during loading). In addition to wave velocity, we estimate the wave amplitude calculated in the frequency domain to exclude the influence of wave dispersion. To obtain wave amplitudes, we calculate the spectrum of each recorded waveform by Fast Fourier Transform (FFT). Since the peak frequency is different for each sample condition and in order to facilitate comparisons, we report the spectral amplitude (A) at a common frequency 400 kHz irrespective of the sample conditions. This frequency is close to the peak frequency across the different sample conditions. We use a piecewise cubic interpolation function to estimate the spectral amplitude at 400kHz as shown in Fig. S3b. The time evolution of the estimated spectral amplitude is shown in Fig. 4e. Consistent with reported observations in literature (Renaud et al., 2012, 2011, 2011, 2010), low-frequency normal stress oscillations result in oscillations in both time shift and spectral amplitude; increasing stress results in a decrease in time shift (increasing wave velocity) and an increase in spectral amplitude (decreasing attenuation). An opposite trend is observed when normal stress decreases. The decrease (increase) in velocity and amplitude during the extensional (compressional) phase is due to the opening (and closing) of compliant features such as micro-cracks and grain boundaries during the oscillations (Rivière et al., 2016).

2.3. Data analysis procedure

We measure the nonlinear elastodynamic response of the Westerly granite sample by quantifying the stress-induced changes in ultrasonic wave velocity and spectral amplitude. Fig. 5 shows a typical response for the saturated-fractured sample under 15-MPa normal stress subjected to a set of 1-MPa dynamic stress oscillations at frequency $f = 1\ Hz$. If the constituent material are linear elastic, ultrasonic wave velocity and amplitude would be stress invariant (i.e., zero nonlinearity). However, even intact rocks exhibit strong nonlinearity. The characteristic nonlinear mesoscopic elastic response of the granite sample includes an instantaneous drop in wave velocity (and amplitude) upon the application of dynamic stress oscillations indicating a sudden elastic softening of the medium also known as conditioning (Johnson and Sutin, 2005). During the stress oscillations, the wave velocity (and amplitude) fluctuates at the frequency of the stress oscillations ($1f$) and its higher harmonics ($nf,\ n = 2,3\ldots,etc.$) and can reach a non-equilibrium steady state, if the oscillations last long enough (fast dynamics). Post oscillation, the wave velocity and amplitude slowly increase (slow dynamics or healing) fully or partially recovering the pre-oscillation values. Fig. 5b-c shows the change in velocity and spectral amplitude as a function of the applied dynamic stress amplitude during the time window marked (green box) in Fig. 5a.

To extract the nonlinearity parameters, we consider that the relative change in velocity is proportional to the change in nonlinear elastic modulus which can be approximated by a second-order polynomial function of strain expressed as (Renaud et al., 2012):

$$2\frac{\Delta c}{c_0} \approx \frac{\Delta M}{M_0} \approx\ O + \beta\varepsilon + \delta\varepsilon^2 \tag{1}$$

where O corresponds to the offset or elastic softening while β and δ are the quadratic and cubic nonlinearity parameters (Guyer and Johnson, 2009). Nonlinearity parameters can be extracted from equation (1) if there is no hysteresis present in the nonlinear signatures. To be able to measure large hysteretic effects and to extract the harmonic contents of the wave velocity, we use a projection procedure following Rivière et al., (2013):

$$\frac{\Delta c}{c_0}(t_j) = R_0 + \sum_{n=1}^{N} A_n \sin(n\omega t_j) + B_n \cos(n\omega t_j) \tag{2}$$

where $R_n = \sqrt{A_n^2 + B_n^2}$ represent the nth harmonic content of the discrete signal of the wave velocity history. The first coefficient R_0 corresponds to the velocity drop or offset. The second coefficient R_1 is the slope or average amplitude of the wave velocity change, which is related to the quadratic nonlinearity parameter (β). The third coefficient R_2 is related to the cubic nonlinearity parameter (δ). We include the first two harmonics (N=2) to obtain the fits shown in Figs. 5b-c. Similarly, the projection procedure is applied to the spectral amplitude history and the corresponding nonlinear parameters are extracted.

We report the following nonlinearity parameters in this paper (1) the velocity drop or R_{0c}; (2) the slope or R_{1c}; (3) The recovery rate of velocity (r_c) post oscillation, assuming a time-logarithmic late time recovery trend in accord with previous observations (Shokouhi et al., 2017b, 2017a; Ten Cate and Shankland, 1996). A similar set of parameters are extracted from the recorded variations in spectral amplitudes, namely R_{0A} and R_{1A} . We measure the pre-oscillation wave velocity (c_0) and pre-oscillation amplitude (A_0) averaged over a 1-second window preceding the oscillations as illustrated in Fig. 5a.

To calculate r_c, we rely on the evolution of wave velocity over a 90-second time window following the termination of each set of

oscillations as shown in Fig. 6. The 90-second waiting time between subsequent oscillations is long enough for most of the relaxation to take place, although the full recovery of the system may take significantly longer (Shokouhi et al., 2017a). The late time recovery follows a time logarithmic trend as shown in Fig. 6b. In order to quantify the recovery rate, the time evolution of wave velocity is described by an equation of the form $c = r_c \log(t) + p$, where r_c is the slope or recovery rate and p is the intercept.

3. Results - Elastic nonlinearity of rock under different normal stress and saturation states

In this section, we compare the measured nonlinearity of the dry-intact, dry-fractured and saturated-fractured samples at the three applied normal stress levels (10, 15 and 20 MPa) based on the nonlinearity parameters R_{0c}, R_{1c}, r_c, R_{0A}, R_{1A}. The results discussed in this section correspond to data measured from the T2-R2 pair for the intact sample and the T3-R3 pair for the dry- and saturated-fractured samples. Fig. 7 shows an example of how the wave velocity and spectral amplitude evolve in response to the imposed normal stress oscillations of varying amplitude and frequency. Fig. 8 shows the calculated R_{0c} as a function of the applied stress oscillation amplitudes ranging from 0.2 MPa to 1 MPa for the three normal stress levels and sample conditions. We observe that the calculated R_{0c} corresponding to the repeated 1-Hz oscillations overlap, indicating the repeatability of the measurements. The occasional differences hint at the possibility of irrecoverable changes in the system during the 10 Hz oscillations applied between the two 1-Hz oscillation sets. Similarly, the R_{0c} results for the repeated 0.4 MPa amplitude oscillations, as shown in the insets of Fig. S4 for dry and saturated-fractured conditions, indicate the occurrence of permanent – although small – changes in the medium due to the large oscillations.

Examining the trends in Fig. 8, we observe that irrespective of the oscillation frequency, applied static normal stress and sample condition, R_{0c} scales linearly with the normal stress amplitude; however, the slope is different for different sample conditions and normal stress levels. This linear dependency with oscillation amplitude has been reported in previous studies and is consistent with a hysteretic nonlinear behavior (Johnson and Sutin, 2005), although the dependency often transitions from quadratic at low strain to linear at larger strain (Pasqualini et al., 2007; Rivière et al., 2015). Also, the velocity drop R_{0c} for the saturated-fractured sample under 20 MPa normal stress and subjected to the 1-Hz normal stress oscillations (Fig. 8i) is comparable (similar order of magnitude) to that reported in our previous study of fractured Westerly granite samples (Shokouhi et al., 2020).

Next, we compare the measured nonlinearity across sample conditions noting that the larger the absolute value of R_{0c} (more negative), the larger is the material nonlinearity. Counterintuitively, at all three normal stress levels, the dry-intact sample exhibits higher nonlinearity than the dry-fractured sample as shown in Fig. 8. This observation is surprising because the presence of the fracture is expected to increase nonlinearity assuming addition of the associated contact acoustic nonlinearity (CAN) to the intact material nonlinearity (Jin et al., 2020, 2018; Solodov et al., 2002). Comparing the nonlinearity of the fractured sample in dry and saturated conditions, the nonlinearity of the saturated sample is generally smaller except at 10 MPa, where we observe an increase in the nonlinearity under saturated conditions.

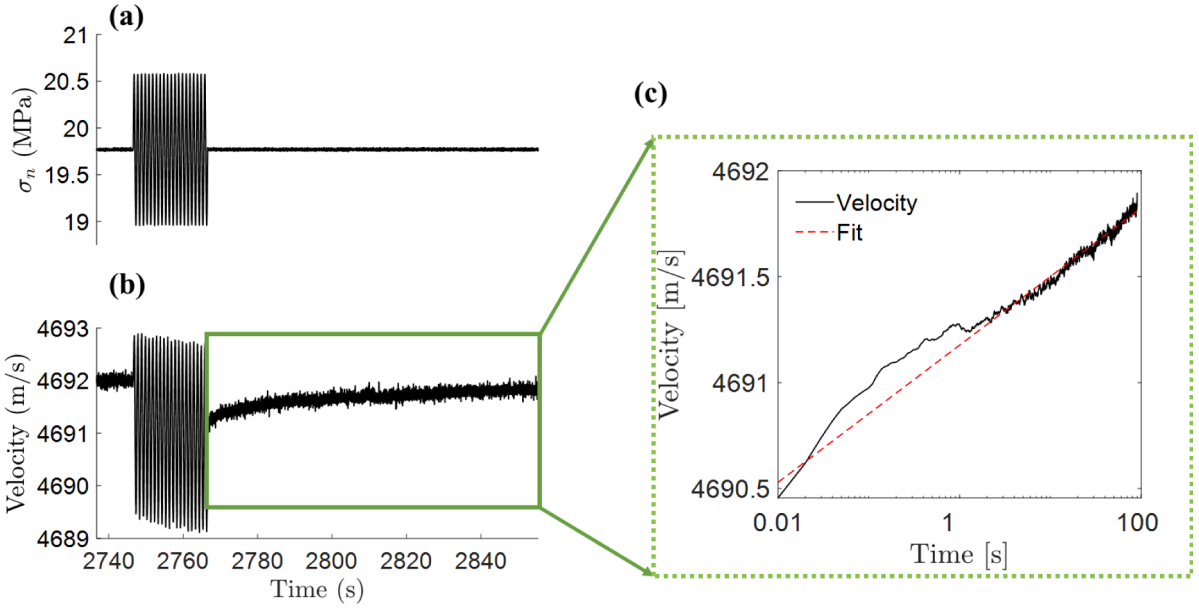

Figure 6. (a) Excerpt from DAET probing of fractured-saturated sample showing the applied normal stress oscillation (amplitude = 0.8 MPa and frequency = 1 Hz) and the corresponding wave velocity changes due to the dynamic stress oscillation. (b) The evolution of wave velocity over the 90 seconds following the termination of the oscillation is used for the recovery analysis (marked by the green box); (c) Recovery of the wave velocity post oscillation plotted as a function of elapsed time (log scale) together with a linear fit $c = r_c \log(t) + p$, where r_c and p are the slope (recovery rate) and intercept, respectively.

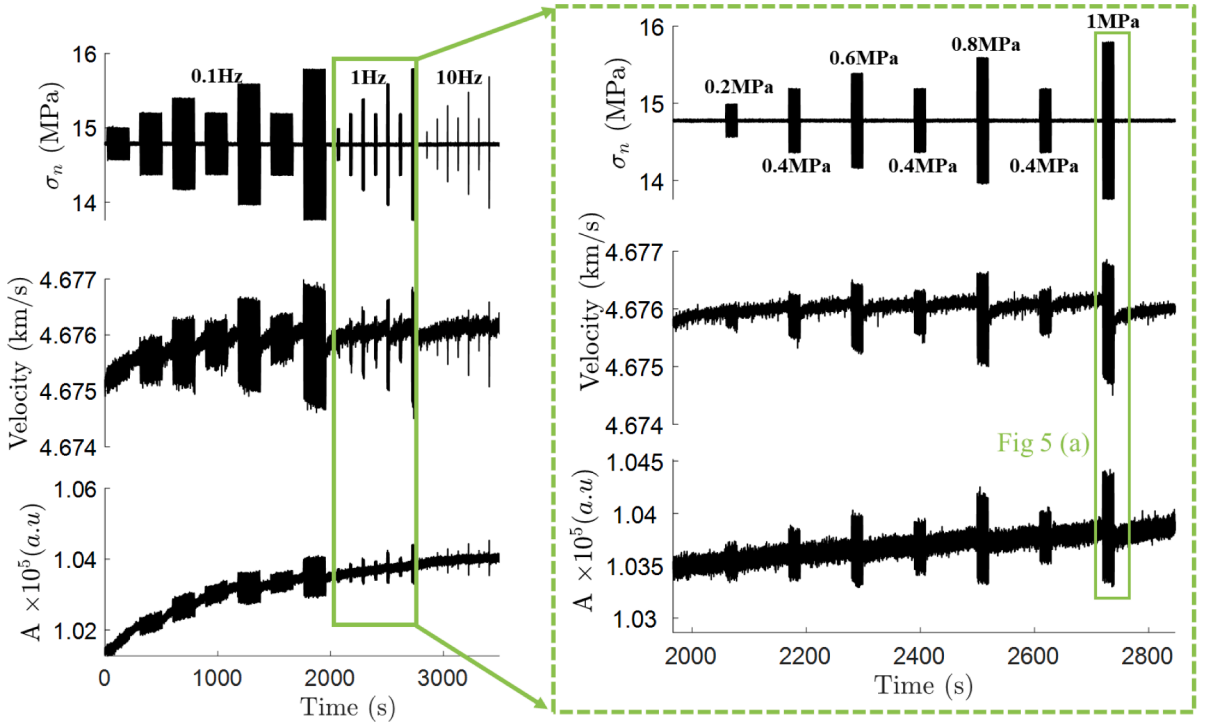

Figure 7. Example of the observed evolution of wave velocity and spectral amplitude (at 400 kHz) due to normal stress oscillations of varying amplitude (0.2 –1.0 MPa) and frequency (0.1 Hz, 1 Hz, 10 Hz) applied to the saturated-fractured sample under a normal stress of 15 MPa. Inset shows the velocity and spectral amplitude for the various normal stress oscillation amplitudes at a common frequency of 1 Hz.

To facilitate a quantitative comparison of the measured nonlinearities at different normal stress levels and for oscillations of different frequencies, we report the slope of R_{0c} vs. stress oscillation amplitude in Fig. 9. Note that the slopes are calculated considering only the first 0.4 MPa amplitude oscillation from the full set, excluding the other two 0.4-MPa amplitude oscillations. The error bars show the uncertainty in the slope of R_{0c} measurement determined using the R^2 value. For the dry-intact sample, the slope tends to increase with increasing oscillation frequency. An observed increase in R_{0c} with increasing oscillation frequency is in accord with previous observations in intact rocks (Rivière et al., 2016). However, for fractured samples we observe different trends at different normal stress levels. An earlier study on saturated fractured rocks reports an increase in R_{0c} with increasing oscillation frequency (Shokouhi et al., 2020), similar to our observation in the saturated-fractured sample at 10 MPa.

Fig. S5 shows R_{1c} as a function of the applied normal stress oscillation amplitudes for the three normal stress levels and sample conditions. The R_{1c} values also scale linearly with the normal stress amplitude, as expected from a quadratic nonlinear behavior (Rivière et al., 2015, 2013). We compute the slope of R_{1c} vs stress oscillation amplitude (Fig. S6) and observe that the slopes appear rather independent of the oscillation frequency at all normal stress levels and sample conditions. This also agrees with the results reported by Rivière et al. (2016) for intact Berea samples. However, previous work on in-situ fractured westerly granite samples report a decreasing trend in the R_{1c} with the oscillation frequency (Shokouhi et al., 2020). Fig. S7 shows the recovery rate (r_c) as a function of applied normal stress oscillation amplitudes. The recovery rate data for the first and second set of 1 Hz oscillation shows significant scatter. Similar to R_{0c} and R_{1c} the recovery rate at all normal stress levels and for all sample conditions scales linearly with the applied normal stress oscillation amplitudes. In addition, the intact sample exhibits steeper recovery rates (i.e., higher nonlinearity) than the dry-fractured sample and the nonlinearity in the saturated-fractured condition is generally lower than that in the intact and dry-fractured samples except at 10 MPa as shown in Fig. S8. These observations taken together suggest that all three parameters R_{0c}, R_{1c} and r_c evolve in a similar fashion and likely arise from similar physical mechanisms.

Fig. 10 shows a similar set of plots for the nonlinearity measured in terms of the spectral amplitude drop R_{0A}. Also, the slope of R_{0A} vs. stress oscillation amplitude is shown in Fig. 11. The trends observed for R_{0A} and R_{0c} are for the large part similar, but there are some differences as well. Similar to R_{0c}, R_{0A} mostly increases linearly with the normal stress oscillation amplitude. However, – in contrast to R_{0c} – R_{0A} for the dry-intact sample monotonically decreases as the normal stress level increases. Also, R_{0A} is consistently smaller for the saturated-fractured sample than the dry-fractured sample at all levels of applied normal stress. Generally, the data pertaining to the dry-fractured condition shows more scatter and the two sets of 1-Hz frequency oscillations do not show good repeatability especially at 10 MPa. This is an indication that some irrecoverable changes might have occurred during the 10 Hz oscillations applied in between the two 1-Hz oscillation sets. Consistent with our earlier observations from velocity-based nonlinearity parameters, the dry-fractured sample exhibits less nonlinearity than the intact sample except at 10 MPa. The unusual trend and large scatter in data at 10 MPa is possibly due to a very low transmission coefficient across a fairly open fracture. Similar to R_{1c}, R_{1A} values also scale linearly with the

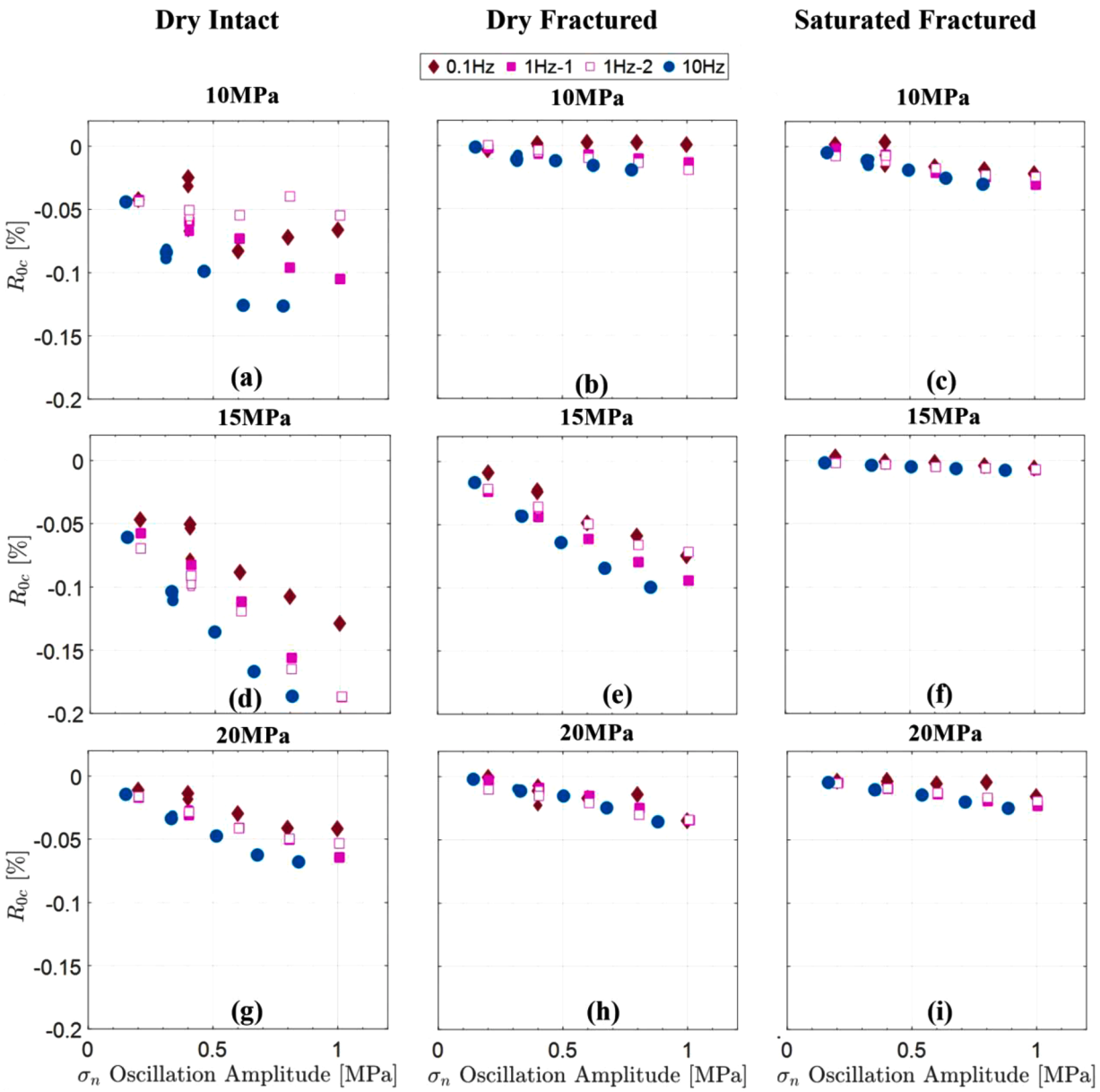

Figure 8. Velocity drop R_{0c} as a function of applied normal stress oscillation amplitude correspond to: (a)-(c) 10 MPa; (d)-(f) 15 MPa and (g)-(i) 20 MPa normal stress levels. Left, middle and right columns correspond to dry-intact, dry-fractured and saturated-fractured conditions, respectively. Each panel includes data corresponding to oscillations at three different frequencies: 0.1, 1.0 and 10 Hz. Note that the 1 Hz oscillations are repeated twice for reproducibility and that the applied normal stress oscillation amplitudes are slightly smaller for the 10 Hz oscillation compared to 0.1 and 1 Hz oscillations. The data shown here correspond to tramsmitter pairs T2-R2 (intact) and T3-R3 (dry- and saturated-fractured).

normal stress amplitude as shown in Fig. S9. In addition, we observe the trends in Fig. S10 are consistent with velocity-based nonlinearity parameters except that saturated fractured sample at 10 MPa also exhibits low nonlinearity in contrast to the observations from velocity-based nonlinearity parameters.

4. Discussion – Impacts of fracture- and saturation-state on nonlinearity

Our main (and surprising) experimental finding is that the (dry) intact sample exhibits higher nonlinearity than the dry-fractured sample and in general, the nonlinearity of the fractured sample, when saturated, is smaller than that of the dry-fractured sample except at 10 MPa normal stress. These observations are largely independent of the choice of nonlinearity parameter. Here, we investigate the observed trends and propose a hypothesis to explain the differences in the measured nonlinearity parameters. We use numerical simulations and estimated "true" contact area distributions to support our arguments.

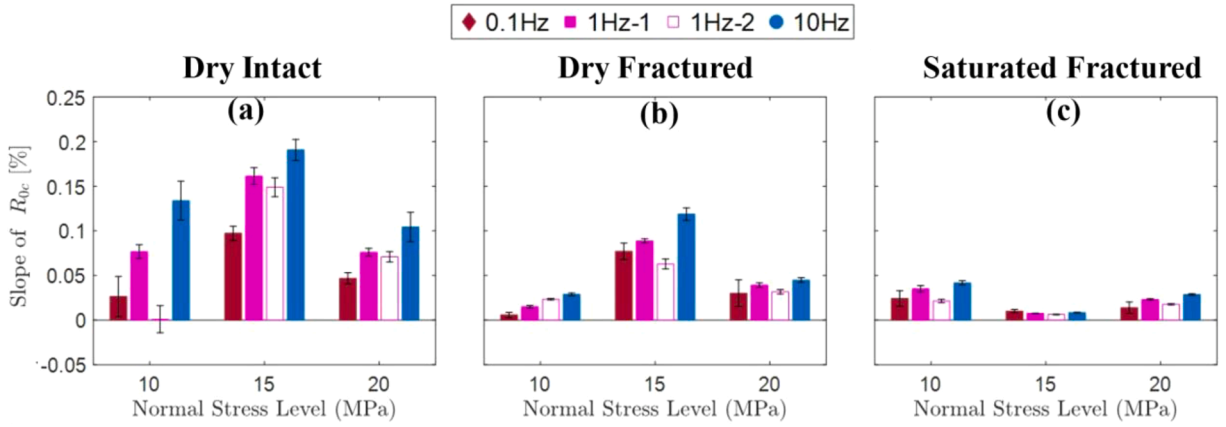

Figure 9. Slope of R_{0c} vs. stress oscillation amplitude at different normal stress levels and frequencies: (a) dry-intact; (b) dry-fractured; and c) saturated-fractured conditions. The error bars show the uncertainty in estimation of the slopes.

4.1. *Variation of nonlinearity with normal stress in dry-intact condition*

In this section, we compare the evolution of nonlinearity parameters with normal stress for intact samples. A decrease in nonlinearity with normal stress is expected due to crack closure and the associated reduction in the pore space connectivity, as reported in dry-intact sandstones (Zinszner et al., 1997, Rivière et al., 2016) for increasing confining pressure (from 0 to ~several tens of MPa). For the pair T2-R2, out of five nonlinear parameters ($R_{0c},\ R_{0A}, R_{1c}, R_{1A},\ r_c$), we see a clear decrease in nonlinearity with normal stress for three of these parameters ($R_{0A},\ R_{1c}$ and R_{1A}). These trends are shown in Figs. 8, 10, S5, S7, S9 for the five NL parameters respectively. For the other two parameters (R_{0c} and r_c), we see a slight increase between 10 and 15 MPa, followed by a decrease between 15 and 20 MPa. It is not immediately clear why nonlinearity increases as normal stress increase from 10 to 15 MPa. One possibility is that compared with previous studies where *confining* pressure was increased, we measure the nonlinearity under *uniaxial* stress oscillations. This slight increase in nonlinearity from 10 to 15 MPa might therefore be due to the opening of initially closed cracks that are oriented parallel to the direction of applied dynamic load. These cracks – completely closed at 10 MPa – might open up slightly at 15 MPa during dynamic oscillations and start contributing to the overall nonlinearity. Recent study has shown that the crack orientation strongly influences the nonlinearity of the medium (TenCate et al., 2016). Also, we note that the nonlinearity evolution with increasing normal stress appears to depend on the local properties of the intact rock. Our measurements of nonlinearity are local and thus depend on the microstructural characteristics of rock volume probed by the ultrasonic wave for a given emitter-receiver pair. The above-discussed behavior pertains to the data measured using the T2-R2 transducer pair. For the other available pair (T1-R1) in intact samples, we find that all nonlinear parameters decrease with increasing normal stress. Fig. S11 shows the nonlinearity measured by R_{0c} using the T1-R1 transducer pair at the three applied normal stress levels.

Finally, observing slightly different trends for the different nonlinearity parameters is not surprising. Although the physical origin of different nonlinearity measures remains elusive, there is empirical evidence suggesting that they arise from different micro-mechanical mechanisms, with R_{1c} (and R_{1A}) on the one hand arising from opening/closing of inter-grain contacts, microcracks and soft inclusions, and other parameters on the other hand arising from other mechanisms (shearing/adhesion, etc) (Rivière et al. 2015, 2016). The anomalous behavior for both r_c and R_{0c} further reinforces the fact that the physical mechanisms for conditioning or elastic softening (R_{0c}) and recovery or slow dynamics (r_c) are similar (Johnson and Sutin, 2005).

4.2. *Effect of pre-oscillation velocity (c_0) and spectral amplitude (A_0) on measured nonlinearities*

Both R_{0c} and R_{0A} evolutions indicate that the intact sample is more nonlinear than the dry and saturated fractured sample (Figs. 8 and 10). As mentioned earlier, this observation is counterintuitive because the presence of the fracture is expected to increase nonlinearity due to addition of the associated contact acoustic nonlinearity (CAN) to the intact materials nonlinearity. It is natural to ask whether this is merely a result of changes in c_0 and A_0. In other words, if the pre-oscillation values of wave velocity and amplitude in the fractured sample are so high compared to those in the intact sample such that the relative changes are lower for the fractured sample. Figs. S12 and S13 show the pre-oscillation velocity c_0 and spectral amplitude A_0 versus the applied stress oscillation amplitudes ranging from 0.2 MPa to 1 MPa for the three normal stress levels and sample conditions. We observe that the pre-oscillation velocity c_0 is indeed between 2.3 % and 13 % larger for the fractured sample at 10 MPa and 15 MPa than that for the intact sample. A similar increase in velocity for fractured rock compared to intact rock sample is reported earlier (Lubbe, 2005; Pyrak-Nolte et al., 1990). However, the measured differences in R_{0c} due to the different c_0 values ($< 13\%$) do not explain the significantly smaller R_{0c} in the dry-fractured sample compared to the intact sample as shown in Figs. 9a-b. Moreover, the pre-oscillation spectral amplitudes are consistently smaller for the fractured sample at all the normal stress levels compared to the intact sample. These observations indicate that the differences in pre-oscillation velocity and amplitude values are insufficient to explain the extent of the decrease in nonlinearity

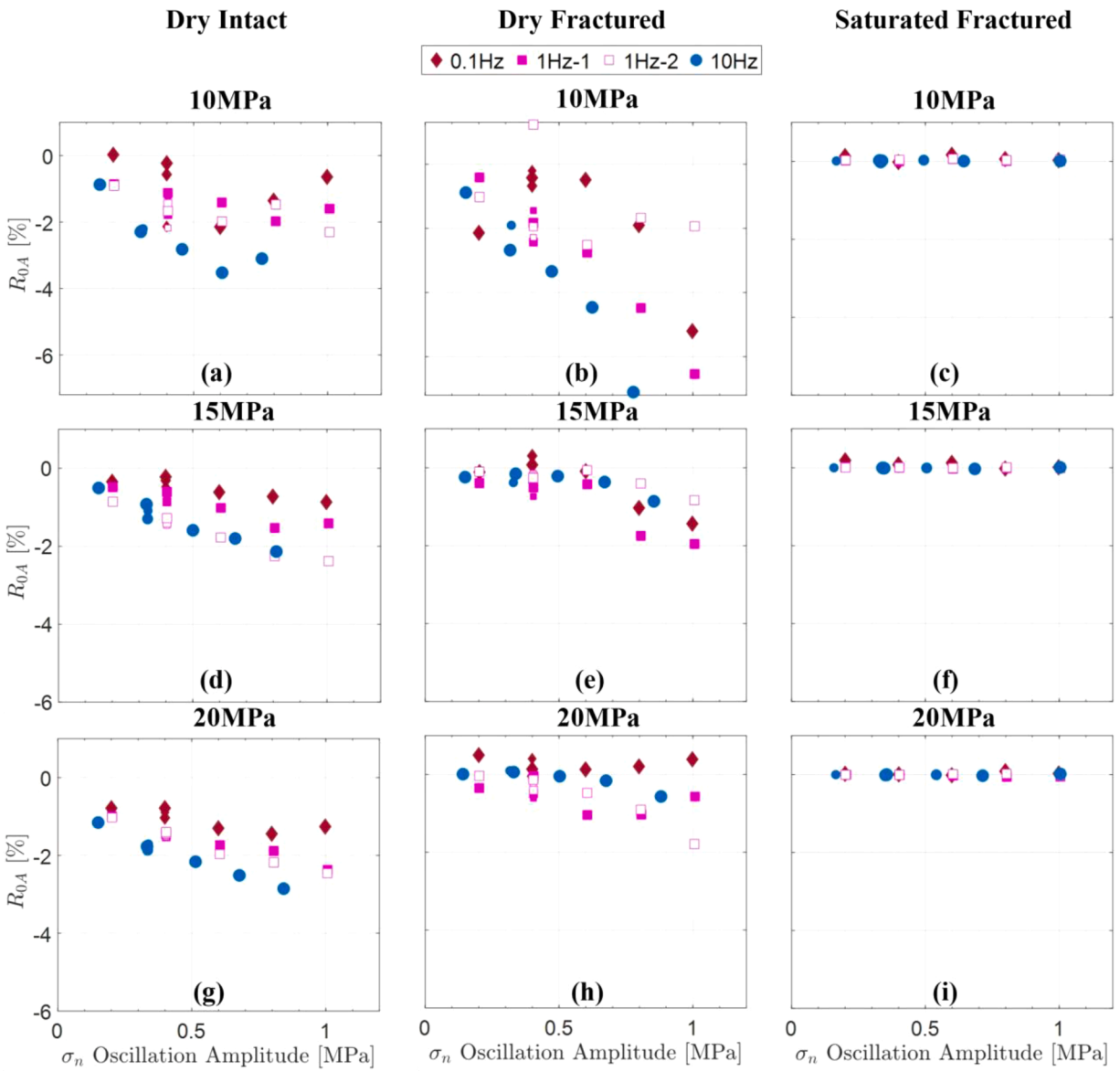

Figure 10. Spectral amplitude drop, R_{0A}, as a function of applied normal stress oscillation amplitude corresponding to mean normal stresses of: (a)-(c) 10 MPa; (d)-(f) 15 MPa and (g)-(i) 20 MPa. Left, middle and right columns correspond to dry-intact, dry-fractured and saturated-fractured conditions, respectively. Each panel includes data for oscillations at three different frequencies: 0.1, 1.0 and 10 Hz. Note that the 1 Hz oscillations are repeated twice. The data correspond to tramsmitter pairs T2-R2 (intact) and T3-R3 (dry- and saturated-fractured).

of the fractured sample compared to that in the intact sample.

4.3. Why the intact sample more nonlinear than the dry-fractured?

We now consider two other potential hypotheses behind the counterintuitive observation that fractured samples appear less nonlinear than intact samples (as shown in Figs. 8, 10, S5, S7 and S9 for the five nonlinearity parameters).

The first one is that the presence of fracture alters the strain distribution across the sample such that only the contacting asperities are strained/compressed sufficiently to contribute to the measured nonlinearity. To investigate the validity of this hypothesis, we conduct a 2D finite element analysis (linear elastic material model) to compare the strain distributions across an intact and a simplified fractured sample using a commercially available finite element software COMSOL Multiphysics® version 5.4 (COMSOL, 2019). Fig. 12a illustrates the details of the numerical model and the applied boundary conditions (BCs). The fracture interface is modeled as a series of half-circular asperities of radius R impinging against a rigid flat surface (Khajeh Salehani et al., 2019). Material properties are chosen to match those of the Westerly granite sample: Young's modulus = 30 GPa, density = 2500 kg/m^3 and Poisson's ratio = 0.3.

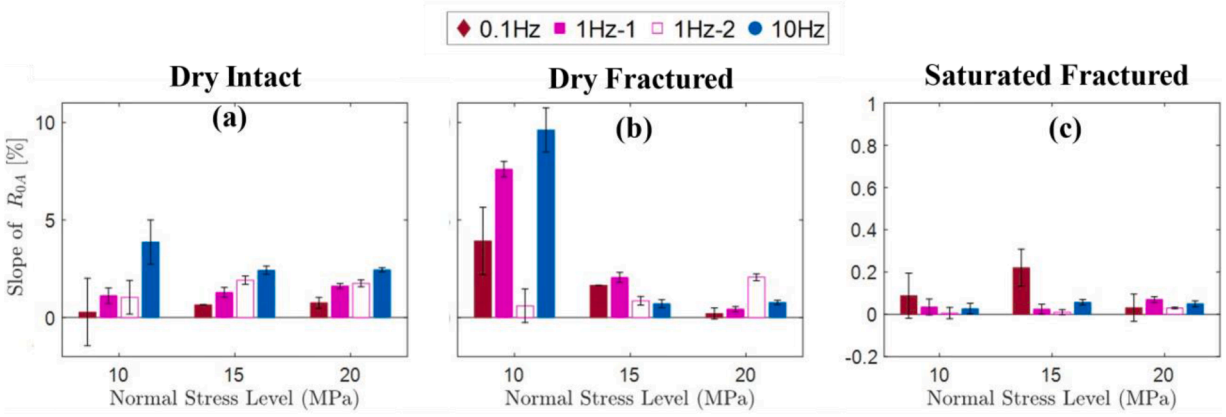

Figure 11. Slope of R_{0A} vs. stress oscillation amplitude at different normal stress levels and frequencies: (a) dry-intact; (b) dry-fractured; and (c) saturated-fractured conditions. The error bars show the uncertainty in the measurement of the slope of R_{0A}.

These values are estimated from the ultrasonic wave velocity of intact Westerly granite. The interaction between the rough and flat surfaces is defined through a contact pair algorithm governed by a penalty method to prevent interpenetration of the separate surfaces. Friction between the surfaces conforms to static Coulomb friction with an interface friction coefficient of 0.3. The mesh is generated automatically corresponding to the 'extremely fine' option with triangular elements an order of magnitude smaller than the shortest wavelength of interest (s-wave). Boundary conditions include a displacement BC applied on one boundary (right-hand side) and a fixed BC on the other (left-hand side) as shown in Fig. 12a. To emulate the experimental condition, we use a two-step approach. The first step is a stationary (static) analysis that simulates the application of normal load by applying a horizontal displacement of 10 μm to the right boundary. The 10-micron displacement produces a uniform stress level of ~15 MPa in the interior of the intact model. In the second step, a *frequency domain* analysis is performed to simulate the response to applied dynamic oscillations. A harmonic perturbation of 3 kN is applied to simulate ~1 MPa dynamic stress in the frequency domain. Similar to the experiments, the oscillation frequency is varied from 1 to 10 Hz in the simulations. The resulting static and dynamic strain fields (ε_{xx} component) are shown in Fig. 12b and 12c, respectively. We present the strain fields across the intact and fractured models with different asperity radii (R) for an oscillation frequency of 10 Hz. Comparing the simulated static strain fields (Fig. 12b), we observe a broadly uniform strain distribution across the intact sample (with an average of $\sim 4 \times 10^{-4}$). For the same displacement BC, the high strain regions in the fractured sample (second column from left, Fig. 12b) are localized around the contacting asperities while strain in the surrounding host rock drops by a factor 2 (down to $\sim 2 \times 10^{-4}$). As the asperity radius increases (third and fourth columns from left), strain in the surrounding host rock continues to decrease. For the single asperity case, static strain in the surrounding host rock becomes an order of magnitude smaller than that in the intact sample (10^{-5} versus 10^{-4}). The dramatic change in the static strain distribution could explain why the nonlinearity appears to be smaller for the fractured sample. First, let us consider a single defect (i.e., a microcrack or grain-grain junction) that contributes to the overall large nonlinearity of the intact sample. After fracture, this defect might become either too closed/strained (if located on/near the fracture plane) or not closed/strained enough (if located far from the fracture plane). In both cases, its contribution to the overall nonlinearity might drop and lead to the apparent drop in the overall nonlinearity. In other words, the microscopic defects in the intact sample might be 'optimally strained' (not too opened, not too closed) to produce a large nonlinearity while becoming unfavorably strained after fracture. Thus, we hypothesize that the disturbance in the static strain field – with highly strained regions localized near the fractured plane and weakly strained regions away from the fractured plane – is what leads to an apparent decrease in nonlinearity.

The reduction in nonlinearity observed after fracture could also be due to a drop in the dynamic strain field (Fig. 12c). Indeed, many studies – often conducted in homogeneous samples – have shown that nonlinearity only arises for strains above a certain threshold (Pasqualini et al., 2007; R. A. Guyer and P. A. Johnson, 2009; Van Den Abeele, 2007). The simulation results in Fig. 12c show that the dynamic strain in the surrounding host rock remains mostly unchanged compared to the intact case (first vs second column from left). However, as the asperity size increases, the dynamic strain field also becomes greatly affected, with highly strained regions near the asperities and weakly strained regions away from the asperities. This trend suggests that changes in the post-fracture dynamic strain field could also contribute to the observed reduction in nonlinearity, especially if the fracture plane is very rough (single asperity case, fourth column).

Overall, these simulation results suggest that the dramatic changes in the static and dynamic strain fields due to fracturing are likely behind the counter-intuitive experimental observations. This interpretation also corroborates previous studies (R. A. Guyer and P. A. Johnson, 2009 and references therein) suggesting that the measured degree of nonlinearity depends on the *strain* the sample experiences (i.e., strain is controlling parameter), as opposed to stress.

We also investigate a second hypothesis that considers the fracture to behave as an acoustic isolator. Specifically, the fractured rock can be represented as a single degree of freedom mass-spring system subjected to harmonic loading. If the excitation frequency (0.1, 1 or 10 Hz) is much higher than the natural frequency of the fractured rock (undamped inertial block spring system), the applied oscillations would be dampened such that the nonlinearity of the fractured medium would not be activated. However, it appears that the

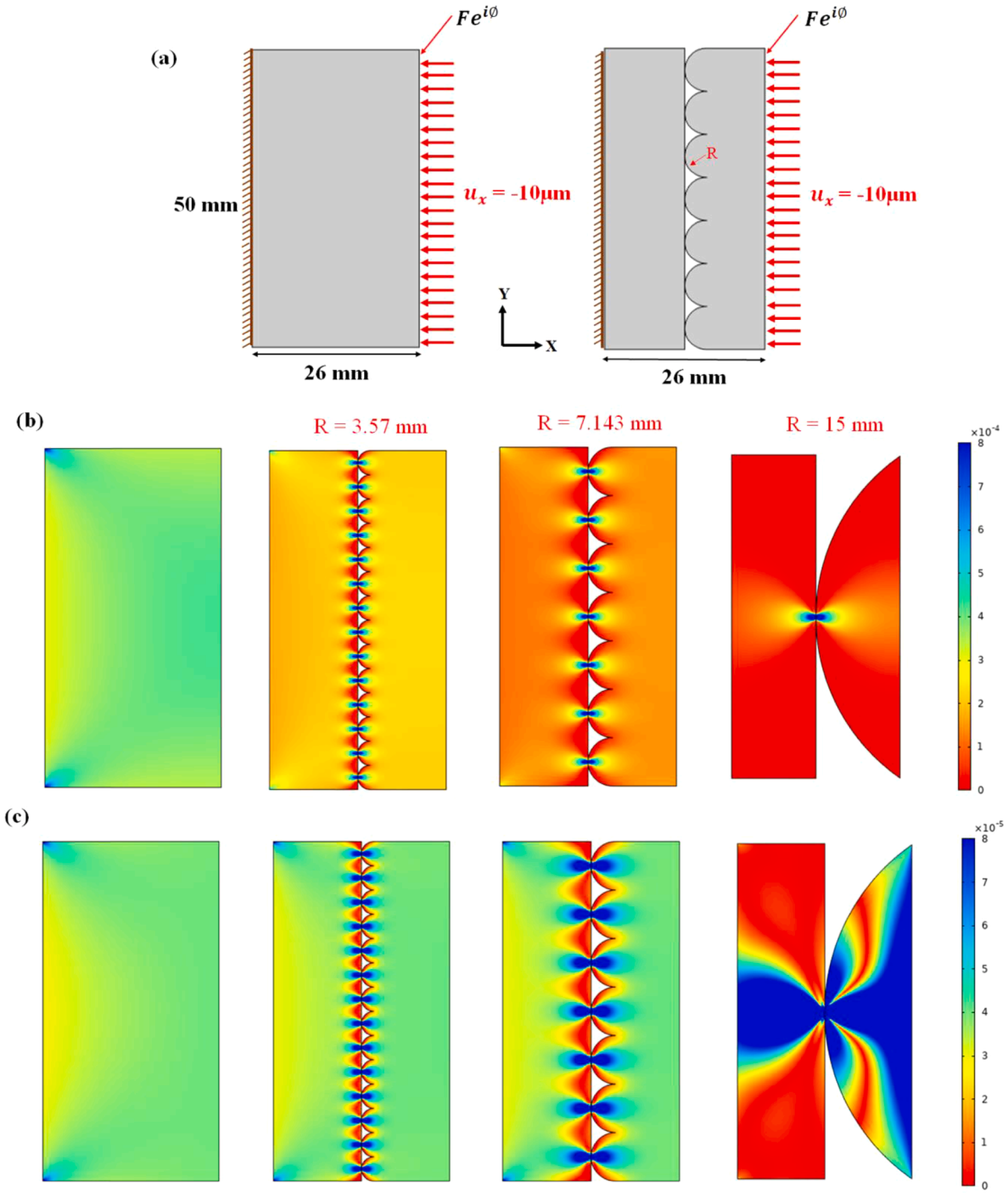

Figure 12. 2D finite element simulation to compare strain distributions in intact and fractured rock: (a) Model geometry and boundary conditions. The asperity radius R is varied to study the effect of asperity size on strain distribution; (b) Simulated static and (c) Simulated dynamic strain field (ε_{xx} component) in the intact sample compared to that for a sample with a fracture modeled as an interface between a flat surface in contact with a rough surface composed of semi-circular asperities of radii R = 3.57 mm, 7.143 mm and 15 mm, respectively.

frequency of normal stress oscillations in our experiments ($\leq$ 10 *Hz*) is an order of magnitude smaller than the natural frequency of the equivalent mass-spring system (~340 kHz). Therefore, we reject this hypothesis as the reason why the fractured sample exhibits a lower nonlinearity than the intact rock.

4.4. Dry vs. saturated fracture

Another important observation is that the saturated-fractured sample is less nonlinear than the dry-fractured sample at 15 and 20 MPa for all five nonlinear measures (Figs. 8, 10, S5, S7 and S9). This is especially true at 15 MPa, and more subtle at 20 MPa. This trend is expected because the presence of a largely incompressible fluid such as water within a tight fracture void is expected to increase the fracture stiffness. Pyrak-Nolte et al. (1990) compare the specific fracture stiffness of naturally fractured samples in both dry and saturated modes and report an increase in dynamic fracture stiffness for saturated samples under axial stresses ranging from 1.4 MPa to 85 MPa. They assert that the increase in stiffness depends on the contact area as well as the aperture and void spaces (Pyrak-Nolte et al., 1990). In addition, the fluid is expected to restrain the movement of the fracture surfaces under the oscillatory perturbation resulting in decreased nonlinearity. Saturating intact rock sample with an incompressible fluid (e.g., water) reduces the pore compressibility and increases the ultrasonic wave velocity (Winkler and McGowan, 2004). Other studies on a variety of intact rock samples report that full saturation reduces nonlinearity (Zinszner et al. (1997), Van den Abeele et al. (2002) and Johnson et al.(2004)). In the case of fractured samples, a decrease in nonlinearity of saturated-fractured steel samples is attributed to the additional stiffness provided by the fluid (Pecorari and Poznic, 2006).

Interestingly, the trend observed at 15 MPa and 20 MPa (discussed above) seems to be reversed at 10 MPa, where the nonlinearity measures are slightly larger when saturated than when dry except for the spectral amplitude-based nonlinearity measures (R_{0A} and R_{1A}). This anomalous observation at 10 MPa is universal irrespective of the T-R pairs (see Fig. S14) or choice of nonlinearity parameter. Although not shown, the trend observed in other nonlinearity parameters is also similar, irrespective of the T-R pairs. We hypothesize that this may be a result of differences in the fracture aperture and contacts at the three different normal stresses. An open fracture with a large aperture is expected to show small at-rest stiffness due to a small contact area. Also, since the fracture is open, the change in contact area (and stiffness) due to small oscillations is very small and therefore, an open fracture will exhibit low nonlinearity. Interestingly, a very tight fracture will also show low nonlinearity due to a large at-rest stiffness and small mobility under oscillations. Jin et al. (2019) demonstrate that discontinuities exhibit high nonlinearity only when they are neither too open nor too closed - falling in a range in between the two extremes. A schematic representation of how nonlinearity varies with stiffness and separation distance (d) between the two fracture surfaces is shown in Fig. 13. This also corroborates results on a semi- infinite crack interface, where the aperture is characterized by a nondimensional gap parameter η varying between zero (crack is fully open) and one (crack is completely closed) (Richardson (1979)). They report that the nonlinearity measured in terms of the second harmonic amplitude is low when η is zero (too open) or one (too closed) and reaches the maximum when η is intermediate at ~0.35.

Fig. 14a shows the estimated distribution of contacts measured using a set of pressure-sensitive films at nominal normal stresses of 10 MPa, 15 MPa and 20 MPa. The approximate area probed by the T3-R3 pair is also marked in Fig. 14a showing that at 10 MPa less than 9% of the nominal contact area is truly in contact for the dry-fractured sample. The percentage area in contact increases to about 13% and 14% at 15 MPa and 20 MPa, respectively. The very low wave transmission (or small spectral amplitudes) at 10 MPa, compared to that at 15 MPa and 20 MPa, as shown in Fig. 14b also suggests that at 10 MPa, the fracture is largely open. Given the prior discussion above, it is not surprising that dry-fractured sample exhibits low nonlinearity. With reference to the schematic of Fig. 13, we hypothesize that the points corresponding to the three different normal stress levels happen to be in three different "nonlinearity regimes". Although the true contact area for the saturated sample at 10 MPa is similar to that for the dry-fractured sample (~9%), we hypothesize that the presence of water in the open fracture at 10 MPa results in an increase in the at-rest fracture stiffness that increases the nonlinearity of the fracture. In contrast, for the fracture at normal stresses of 15 MPa and 20 MPa, the fluid-induced increase in fracture stiffness lowers the nonlinearity from relatively high to low, typical of very tight fractures (see Fig. 14). Pecorari and Poznic (2006) provide an alternative explanation for the unusual behavior observed in their study of dry and water-confined steel interfaces. The nonlinearity (measured in terms of the second harmonic amplitude) of a water-confined steel surface steeply rises within a confining pressure range of ~5 MPa followed by a decrease in the nonlinearity as the pressure increases. They argue that the additional stiffness provided by the water alone cannot explain the initial increase in the nonlinearity. The increasing/decreasing trend is attributed instead to the repulsive surface forces that exist between the water-confined surfaces which seems to enhance the nonlinearity in sample under small pressures (less than 5 MPa) and to decrease the nonlinearity at higher pressures.

5. Conclusion

We report on a series of laboratory experiments designed to investigate how fracturing and saturation modify the nonlinear elastodynamic response of Westerly granite under in-situ stress. The stress-induced changes in the wave velocity and spectral amplitude are evaluated to study the nonlinear elastodynamic response. Our results show that surprisingly, the intact sample exhibits higher nonlinearity than the fractured sample. Using numerical simulations to support our hypothesis, we attribute this counterintuitive finding to the drastic changes in the strain field. The rather constant strain field in the intact sample becomes non-uniform after fracturing, with highly strained regions on the fracture plane and weakly-strained regions in the surrounding host rock. The decrease in nonlinearity after fracture suggests that microscopic defects that were optimally strained before fracturing (neither too opened nor too closed) and contributed to the nonlinearity of the intact sample become unfavorably strained after fracture, i.e., they become either too strained if located on the fracture plane, or not strained enough if located away from the fracture, both leading to a reduction in nonlinearity. In addition, the saturated samples exhibit less nonlinearity than when dry, due to the additional stiffness provided by the fluid within the interface except at low normal stress (10 MPa) when the fracture is open and poromechanically-drained. We attribute this observation to the differences in fracture apertures and consequently, the true contact areas and at-rest fracture stiffnesses at different normal stresses in the dry vs. saturated conditions. Our findings suggest the complexity of the physical mechanisms behind

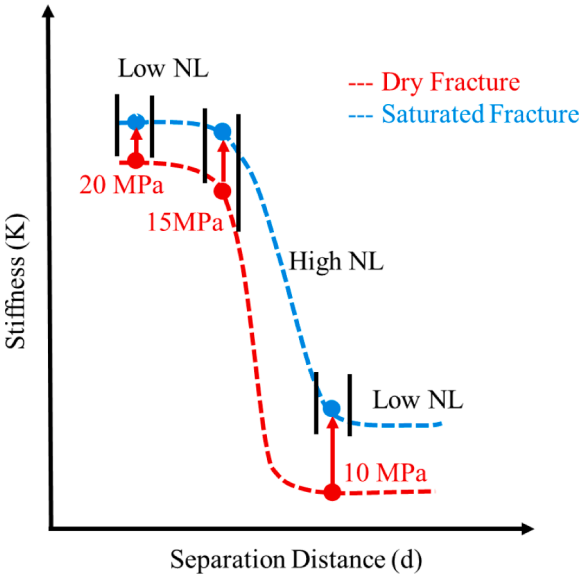

Figure 13. Schematic representation of the relationship between contact acoustic nonlinearity, at rest stiffness (K) and separation distance (d) between two fracture surfaces. Fractured medium exhibits high nonlinearity when the separation distance or stiffness is neither too large nor too small, falling in a range between the two extremes. Response of dry and saturated fractures showing that the three different normal stress levels fall in different "nonlinearity regimes". The two black lines surrounding each point indicate the portion of the K(d) curve explored during normal stress oscillations.

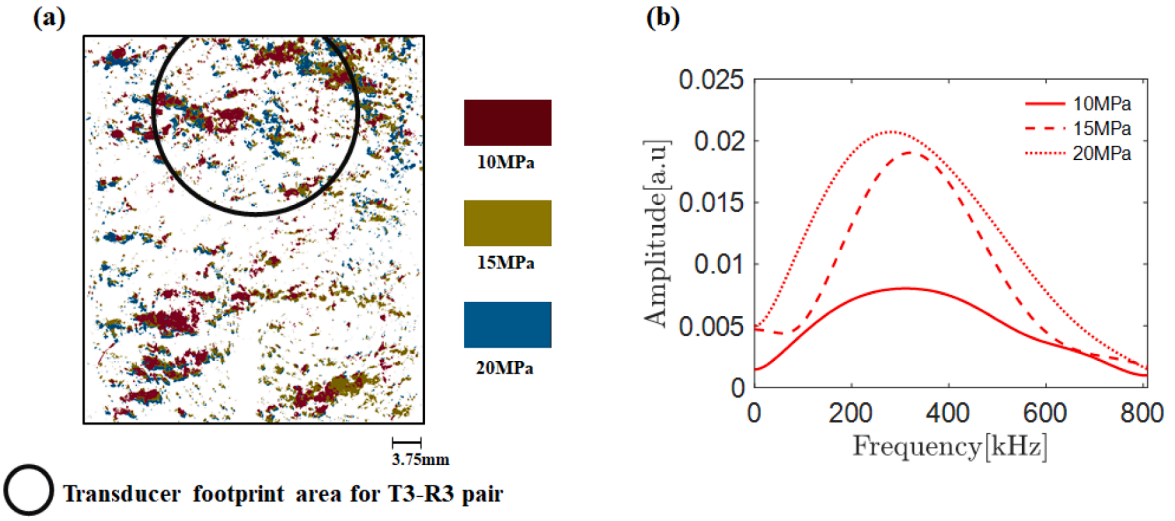

Figure 14. The "true" distribution of contacts estimated at three different normal stress levels using a series of pressure senstitive films for the dry-fractured sample.The circle shows the approximate area probed by the T3-R3 PZT pair accommodating beam spread for a transducer diameter of 6.5 mm and center frequency of 500 kHz. (b) Measured spectral amplitude of dry-fractured sample at the three normal stress levels. Data shown are for the T3-R3 PZT pair.

the nonlinear elastodynamic response of fractured rocks under stress including the role of fracture aperture and contact area.

Our future experiments involve saw-cut samples of known roughness to decouple the influence of fracture aperture and roughening in modifying the nonlinear elastodynamic response. Using a simpler system will help reveal underlying mechanisms of nonlinearity. In addition, we plan to use the data to extend the existing analytical models (Jin et al., 2020) taking into account the effect of friction and saturation. A better understanding of the nonlinear elastodynamic behavior of fractured rock is crucial in exploiting the coupling between nonlinear stiffness and permeability change to predict the poromechanical properties of rock. This coupling will enable remote characterization of the hydraulic response of fractured rock from seismic data with broad application in managing engineered geothermal systems, waste storage, and unconventional reservoirs.

Declaration of competing interest

The authors declare that they have no known competing financial interests or personal relationships that could have appeared to influence the work reported in this paper.

Acknowledgment

This material is based upon work supported by the U.S. Department of Energy, Office of Science, Office of Basic Energy Sciences Energy Frontier Research Centers program under Award Number DE-SC-0001234. We thank S. Swavely for assistance in the laboratory.

Author Agreement Statement

None.

Supplementary materials

Supplementary material associated with this article can be found, in the online version, at doi:10.1016/j.jmps.2021.104491.

References

Bandis, S.C., Lumsden, A.C., Barton, N.R., 1983. Fundamentals of rock joint deformation. Int. J. Rock Mech. Min. Sci. Geomech. Abstr. 20, 249–268. https://doi.org/10.1016/0148-9062(83)90595-8.

Berkowitz, B., 2002. Characterizing flow and transport in fractured geological media: A review. Adv. Water Resour. 25, 861–884. https://doi.org/10.1016/S0309-1708(02)00042-8.

Brenguier, F., Campillo, M., Hadziioannou, C., Shapiro, N.M., Nadeau, R.M., Larose, E., 2008. Postseismic relaxation along the san andreas fault at Parkfield from continuous seismological observations. science (80-.). 321, 1478–1481. doi:10.1126/science.1160943.

Brenguier, F., Campillo, M., Takeda, T., Aoki, Y., Shapiro, N.M., Briand, X., Emoto, K., Miyake, H., 2014. Mapping pressurized volcanic fluids from induced crustal seismic velocity drops. Science 345 (80-), 80–82. https://doi.org/10.1126/science.1254073.

Brown, S.R., 1987. Fluid flow through rock joints: the effect of surface roughness. J. Geophys. Res. 92, 1337. https://doi.org/10.1029/JB092iB02p01337.

Candela, T., Brodsky, E.E., Marone, C., Elsworth, D., 2015. Flow rate dictates permeability enhancement during fluid pressure oscillations in laboratory experiments. J. Geophys. Res. Solid Earth 120, 2037–2055. https://doi.org/10.1002/2014JB011511.

COMSOL, 2019. Multiphysics Reference Manual, Version 5, 4. COMSOL, Inc. www.comsol.com.

Elkhoury, J.E., Brodsky, E.E., Agnew, D.C., 2006. Seismic waves increase permeability. Nature 441, 1135–1138. https://doi.org/10.1038/nature04798.

Elkhoury, J.E., Niemeijer, A., Brodsky, E.E., Marone, C., 2011. Laboratory observations of permeability enhancement by fluid pressure oscillation of in situ fractured rock. J. Geophys. Res. 116, B02311. https://doi.org/10.1029/2010JB007759.

Gassenmeier, M., Sens-Schönfelder, C., Eulenfeld, T., Bartsch, M., Victor, P., Tilmann, F., Korn, M., 2016. Field observations of seismic velocity changes caused by shaking-induced damage and healing due to mesoscopic nonlinearity. Geophys. J. Int. 204, 1490–1502. https://doi.org/10.1093/gji/ggv529.

Guyer, R.A., Johnson, P.A., 2009. Nonlinear Mesoscopic Elasticity, Nonlinear Mesoscopic Elasticity. Wiley. https://doi.org/10.1002/9783527628261.

Haupert, S., Renaud, G., Rivière, J., Talmant, M., Johnson, P.A., Laugier, P., 2011. High-accuracy acoustic detection of nonclassical component of material nonlinearity. J. Acoust. Soc. Am. 130, 2654–2661. https://doi.org/10.1121/1.3641405.

Holcomb, D.J., 1981. Memory, relaxation, and microfracturing in dilatant rock. J. Geophys. Res. Solid Earth 86, 6235–6248. https://doi.org/10.1029/JB086iB07p06235.

Hudson, J.A., Liu, E., Crampin, S., 1996. The mechanical properties of materials with interconnected cracks and pores. Geophys. J. Int. 124, 105–112. https://doi.org/10.1111/j.1365-246X.1996.tb06355.x.

Jin, J., 2019. The Correspondence Between Microstructural Features and Acoustic Nonlinearity. PhD thesis. Pennsylvania State University, United States.

Jin, J., Johnson, P., Shokouhi, P., 2020. An integrated analytical and experimental study of contact acoustic nonlinearity at rough interfaces of fatigue cracks. J. Mech. Phys. Solids 135, 103769. https://doi.org/10.1016/j.jmps.2019.103769.

Jin, J., Rivière, J., Ohara, Y., Shokouhi, P., 2018. Dynamic acousto-elastic response of single fatigue cracks with different microstructural features: an experimental investigation. J. Appl. Phys. 124 https://doi.org/10.1063/1.5036531.

Johnson, P., Sutin, A., 2005. Slow dynamics and anomalous nonlinear fast dynamics in diverse solids. J. Acoust. Soc. Am. 117, 124–130. https://doi.org/10.1121/1.1823351.

Johnson, P.A., Bodin, P., Gomberg, J., Pearce, F., Lawrence, Z., Menq, F.-Y., 2009. Inducing in situ, nonlinear soil response applying an active source. J. Geophys. Res. 114, B05304. https://doi.org/10.1029/2008JB005832.

Johnson, P.A., Zinszner, B., Rasolofosaon, P., Cohen-Tenoudji, F., Van Den Abeele, K., 2004. Dynamic measurements of the nonlinear elastic parameter α in rock under varying conditions. J. Geophys. Res. Solid Earth 109. https://doi.org/10.1029/2002JB002038.

Khajeh Salehani, M., Irani, N., Nicola, L., 2019. Modeling adhesive contacts under mixed-mode loading. J. Mech. Phys. Solids 130, 320–329. https://doi.org/10.1016/j.jmps.2019.06.010.

Lott, M., Remillieux, M.C., Le Bas, P.-Y., Ulrich, T.J., Garnier, V., Payan, C., 2016. From local to global measurements of nonclassical nonlinear elastic effects in geomaterials. J. Acoust. Soc. Am. 140, EL231–EL235. https://doi.org/10.1121/1.4962373.

Lubbe, R., 2005. A field and laboratory investigation of the compliance of fractured rock. University of Oxford.

Nakata, N., Snieder, R., 2011. Near-surface weakening in Japan after the 2011 Tohoku-Oki earthquake. Geophys. Res. Lett. 38 https://doi.org/10.1029/2011GL048800 n/a-n/a.

Nara, Y., Meredith, P.G., Yoneda, T., Kaneko, K., 2011. Influence of macro-fractures and micro-fractures on permeability and elastic wave velocities in basalt at elevated pressure. Tectonophysics 503, 52–59. https://doi.org/10.1016/j.tecto.2010.09.027.

Niu, F., Silver, P.G., Daley, T.M., Cheng, X., Majer, E.L., 2008. Preseismic velocity changes observed from active source monitoring at the Parkfield SAFOD drill site. Nature 454, 204–208. https://doi.org/10.1038/nature07111.

Pasqualini, D., Heitmann, K., TenCate, J.A., Habib, S., Higdon, D., Johnson, P.A., 2007. Nonequilibrium and nonlinear dynamics in Berea and Fontainebleau sandstones: Low-strain regime. J. Geophys. Res. 112, B01204. https://doi.org/10.1029/2006JB004264.

Pecorari, C., Poznic, M., 2006. On the linear and nonlinear acoustic properties of dry and water-confining elasto-plastic interfaces. Proc. R. Soc. A Math. Phys. Eng. Sci. 462, 769–788. https://doi.org/10.1098/rspa.2005.1595.
Pyrak-Nolte, L.J., Myer, L.R., Cook, N.G.W., 1990. Transmission of seismic waves across single natural fractures. J. Geophys. Res. 95, 8617. https://doi.org/10.1029/JB095iB06p08617.
Pyrak-Nolte, L.J., Nolte, D.D., 2016. Approaching a universal scaling relationship between fracture stiffness and fluid flow. Nat. Commun. 7, 10663. https://doi.org/10.1038/ncomms10663.
Guyer, R.A., Johnson, P.A., 2009. Nonlinear Mesoscopic Elasticity: The Complex Behavior of Rocks, Soil, and Concrete. Wiley, Weinheim, p. 2009.
Remillieux, M.C., Guyer, R.A., Payan, C., Ulrich, T.J., 2016. Decoupling nonclassical nonlinear behavior of elastic wave types. Phys. Rev. Lett. 116, 1–5. https://doi.org/10.1103/PhysRevLett.116.115501.
Renaud, G., Callé, S., Defontaine, M., 2010. Dynamic acoustoelastic testing of weakly pre-loaded unconsolidated water-saturated glass beads. J. Acoust. Soc. Am. 128, 3344–3354. https://doi.org/10.1121/1.3502461.
Renaud, G., Le Bas, P.-Y., Johnson, P.A., 2012. Revealing highly complex elastic nonlinear (anelastic) behavior of Earth materials applying a new probe: dynamic acoustoelastic testing. J. Geophys. Res. Solid Earth 117. https://doi.org/10.1029/2011JB009127 n/a-n/a.
Renaud, G, Rivière, J., Haupert, S., Laugier, P., 2013. Anisotropy of dynamic acoustoelasticity in limestone, influence of conditioning, and comparison with nonlinear resonance spectroscopy. J. Acoust. Soc. Am. 133, 3706–3718. https://doi.org/10.1121/1.4802909.
Renaud, G., Rivière, J., Larmat, C., Rutledge, J.T., Lee, R.C., Guyer, R.A., Stokoe, K., Johnson, P.A., 2014. In situ characterization of shallow elastic nonlinear parameters with Dynamic Acoustoelastic Testing. J. Geophys. Res. Solid Earth 119, 6907–6923. https://doi.org/10.1002/2013JB010625.
Renaud, G., Rivière, J., Le Bas, P.-Y., Johnson, P.A., 2013. Hysteretic nonlinear elasticity of Berea sandstone at low-vibrational strain revealed by dynamic acousto-elastic testing. Geophys. Res. Lett. 40, 715–719. https://doi.org/10.1002/grl.50150.
Renaud, G., Talmant, M., Callé, S., Defontaine, M., Laugier, P., 2011. Nonlinear elastodynamics in micro-inhomogeneous solids observed by head-wave based dynamic acoustoelastic testing. J. Acoust. Soc. Am. 130, 3583–3589. https://doi.org/10.1121/1.3652871.
Renaud, G., Talmant, M., Marrelec, G., 2016. Microstrain-level measurement of third-order elastic constants applying dynamic acousto-elastic testing. J. Appl. Phys. 120, 135102 https://doi.org/10.1063/1.4963829.
Richardson, J.M., 1979. Harmonic generation at an unbonded interface—I. Planar interface between semi-infinite elastic media. Int. J. Eng. Sci. 17, 73–85. https://doi.org/10.1016/0020-7225(79)90008-9.
Rivière, J., Pimienta, L., Scuderi, M., Candela, T., Shokouhi, P., Fortin, J., Schubnel, A., Marone, C., Johnson, P.A., 2016. Frequency, pressure, and strain dependence of nonlinear elasticity in Berea Sandstone. Geophys. Res. Lett. 43, 3226–3236. https://doi.org/10.1002/2016GL068061.
Rivière, J., Remillieux, M.C., Ohara, Y., Anderson, B.E., Haupert, S., Ulrich, T.J., Johnson, P.A., 2014. Dynamic acousto-elasticity in a fatigue-cracked sample. J. Nondestruct. Eval. 33, 216–225. https://doi.org/10.1007/s10921-014-0225-0.
Rivière, J., Renaud, G., Guyer, R.A., Johnson, P.A., 2013. Pump and probe waves in dynamic acousto-elasticity: Comprehensive description and comparison with nonlinear elastic theories. J. Appl. Phys. 114, 054905 https://doi.org/10.1063/1.4816395.
Rivière, J., Shokouhi, P., Guyer, R.a, Johnson, P.a, 2015. Journal of geophysical research : solid earth a set of measures for the systematic classification of the nonlinear elastic behavior of disparate rocks. J. Geophys. Res. Solid Earth 120, 1587–1604. https://doi.org/10.1002/2014JB011718.Received.
Rubinstein, J.L., 2004. Evidence for widespread nonlinear strong ground motion in the MW 6.9 loma prieta earthquake. Bull. Seismol. Soc. Am. 94, 1595–1608. https://doi.org/10.1785/012004009.
Samuelson, J., Elsworth, D., Marone, C., 2009. Shear-induced dilatancy of fluid-saturated faults: experiment and theory. J. Geophys. Res. 114, B12404. https://doi.org/10.1029/2008JB006273.
Schneider, C.A., Rasband, W.S., Eliceiri, K.W., 2012. NIH Image to ImageJ: 25 years of image analysis. Nat. Methods 9, 671–675. https://doi.org/10.1038/nmeth.2089.
Selvadurai, P.A., Glaser, S.D., 2017. Asperity generation and its relationship to seismicity on a planar fault: a laboratory simulation. Geophys. J. Int. 208, 1009–1025. https://doi.org/10.1093/gji/ggw439.
Sens-Schönfelder, C., Eulenfeld, T., 2019. Pobing the in situ Elastic Nonlinearity of Rocks with Earth Tides and Seismic Noise. Phys. Rev. Lett 122,138501. https://doi.org/10.1103/PhysRevLett.122.138501.
Sens-Schönfelder, C., Snieder, R., Li, X., 2018. A model for nonlinear elasticity in rocks based on friction of internal interfaces and contact aging. Geophys. J. Int. 216, 319–331. https://doi.org/10.1093/gji/ggy414.
Shokouhi, P., Jin, J., Wood, C., Rivière, J., Madara, B., Elsworth, D., Marone, C., 2020. Dynamic stressing of naturally fractured rocks: on the relation between transient changes in permeability and elastic wave velocity. Geophys. Res. Lett. 47, 1–10. https://doi.org/10.1029/2019GL083557.
Shokouhi, P., Rivière, J., Guyer, R.A., Johnson, P.A., 2017a. Slow dynamics of consolidated granular systems: multi-scale relaxation. Appl. Phys. Lett. 111 https://doi.org/10.1063/1.5010043.
Shokouhi, P., Rivière, J., Lake, C.R., Le Bas, P.Y., Ulrich, T.J., 2017b. Dynamic acousto-elastic testing of concrete with a coda-wave probe: comparison with standard linear and nonlinear ultrasonic techniques. Ultrasonics 81, 59–65. https://doi.org/10.1016/j.ultras.2017.05.010.
Solodov, I.Y., Krohn, N., Busse, G., 2002. CAN: an example of nonclassical acoustic nonlinearity in solids. Ultrasonics 40, 621–625. https://doi.org/10.1016/S0041-624X(02)00186-5.
Ten Cate, J.A., Shankland, T.J., 1996. Slow dynamics in the nonlinear elastic response of Berea sandstone. Geophys. Res. Lett. 23, 3019–3022. https://doi.org/10.1029/96gl02884.
TenCate, J.A., Malcolm, A.E., Feng, X., Fehler, M.C., 2016. The effect of crack orientation on the nonlinear interaction of a P wave with an S wave. Geophys. Res. Lett. 43, 6146–6152. https://doi.org/10.1002/2016GL069219.
TenCate, J.A., Smith, E., Guyer, R.A., 2000. Universal Slow Dynamics in Granular Solids. Phys. Rev. Lett. 85, 1020–1023. https://doi.org/10.1103/PhysRevLett.85.1020.
Van Den Abeele, K.E.-A., 2002. Influence of water saturation on the nonlinear elastic mesoscopic response in Earth materials and the implications to the mechanism of nonlinearity. J. Geophys. Res. 107, 1–11. https://doi.org/10.1029/2001jb000368.
Van Den Abeele, K., 2007. Multi-mode nonlinear resonance ultrasound spectroscopy for defect imaging: An analytical approach for the one-dimensional case. J. Acoust. Soc. Am. 122, 73–90. https://doi.org/10.1121/1.2735807.
Van Den Abeele, K.E.-A., Carmeliet, J., Ten Cate, J.A., Johnson, P.A., 2000. Nonlinear Elastic Wave Spectroscopy (NEWS) Techniques to Discern Material Damage, Part II: Single-Mode Nonlinear Resonance Acoustic Spectroscopy. Res. Nondestruct. Eval. 12, 31–42. https://doi.org/10.1080/09349840009409647.
Wegler, U., Nakahara, H., Sens-Schönfelder, C., Korn, M., Shiomi, K., 2009. Sudden drop of seismic velocity after the 2004 M w 6.6 mid-Niigata earthquake, Japan, observed with Passive Image Interferometry. J. Geophys. Res. 114, B06305. https://doi.org/10.1029/2008JB005869.
Winkler, K.W., Liu, X., 1996. Measurements of third-order elastic constants in rocks. J. Acoust. Soc. Am. 100, 1392–1398. https://doi.org/10.1121/1.415986.
Winkler, K.W., McGowan, L., 2004. Nonlinear acoustoelastic constants of dry and saturated rocks. J. Geophys. Res. Solid Earth 109, 1–9. https://doi.org/10.1029/2004JB003262.
Zinszner, B., Johnson, P.A., Rasolofosaon, P.N.J., 1997. Influence of change in physical state on elastic nonlinear response in rock: Significance of effective pressure and water saturation. J. Geophys. Res. Solid Earth 102, 8105–8120. https://doi.org/10.1029/96JB03225.